


RESEARCH ARTICLE

Extension and application of an observation-based local climate index aimed to anticipate the impact of El Niño–Southern Oscillation events on Colombia

Juan-Manuel Sayol¹  | Laura M. Vásquez² | Jorge L. Valencia² |
Jean R. Linero-Cueto³ | David García-García¹ | Isabel Vigo¹ | Alejandro Orfila⁴

¹Department of Applied Mathematics, University of Alicante, Alicante, Spain

²Dirección General Marítima, Centro de Investigaciones Oceanográficas e Hidrográficas del Pacífico, Tumaco, Colombia

³Facultad de Ingeniería, Universidad del Magdalena, Santa Marta, Colombia

⁴Instituto Mediterráneo de Estudios Avanzados (CSIC-UIB), Esporles, Spain

Correspondence

Juan-Manuel Sayol, Department of Applied Mathematics, University of Alicante, 03690 Sant Vicent del Raspeig, Alicante, Spain.
Email: juanma.sayol@ua.es

Funding information

FEDER/Ministerio de Ciencia, Innovación y Universidades – Agencia Estatal de Investigación, Grant/Award Number: RTI2018-093941-B-C31; Generalitat Valenciana and the European Social Fund, Grant/Award Number: APOSTD/2020/254; Ministry of National Defense of Colombia; Governorate of Magdalena (Colombia); FEDER/Ministerio de Ciencia, Innovación y Universidades - Agencia Estatal de Investigación, Grant/Award Number: RTI2018-093874-B-100; Generalitat Valenciana, Grant/Award Number: Prometeo PROMETEO/2021/030

Abstract

The Tumaco multivariate index (TMI) is a multidecadal monthly index constructed with unique time series of sea surface temperature, surface air temperature and rain measured at Tumaco bay, in the southern Pacific coast of Colombia, and available since 1961. In this work, this index is re-evaluated after the addition of in situ sea level data, and its properties for different standardization periods are compared against oceanic El Niño–Southern Oscillation (ENSO) and other derived indices. In particular, we propose a modified TMI, hereinafter referred as TMI4, whose potential to identify the expected sign and the amount of future variations of rain induced by ENSO events in Colombia is analysed for selected extreme episodes. Results indicate that after the inclusion of sea level data, TMI4 can anticipate the development of El Niño events before the ENSO 3 and some other sea surface temperature-based regional indices, although its predictability depends on the ENSO type (canonical or Modoki). The explanation is that sea level includes new information into TMI4 on the onset of El Niño events. In particular, the signal of intraseasonal sea level anomalies carried by downwelling Kelvin waves is detected at Tumaco tide-gauge. Moreover, the analysis of the differences, both in magnitude and spatial distribution, of rainfall anomalies induced by positive (El Niño) and negative (La Niña) ENSO events characterized by TMI4 are regionally presented. As a result, we find that TMI4 is especially suited for extensive northern and western areas of mainland Colombia. For completeness, in the appendix we briefly introduce the semi-automated implementation of TMI4, including a visual interface, which is currently being tested by personnel within the operational oceanography area at Centro de Investigaciones Oceanográficas e Hidrográficas del Pacífico (Dimar-CCCP).

Abbreviations: CLLJ, Caribbean low-level jet; ENSO, El Niño–Southern Oscillation; TMI, Tumaco multivariate index; TMI4, modified Tumaco multivariate index.

This is an open access article under the terms of the [Creative Commons Attribution-NonCommercial](https://creativecommons.org/licenses/by-nc/4.0/) License, which permits use, distribution and reproduction in any medium, provided the original work is properly cited and is not used for commercial purposes.

© 2022 The Authors. *International Journal of Climatology* published by John Wiley & Sons Ltd on behalf of Royal Meteorological Society.

KEYWORDS

Colombia, El Niño, El Niño–Southern Oscillation, equatorial Kelvin waves, La Niña, modified Tumaco multivariate index, rainfall forecasting, Tumaco multivariate index

1 | INTRODUCTION

Floods and droughts are among the natural hazards that higher economic loss and more human deaths cause on the Earth (e.g., Raikes *et al.*, 2019; He *et al.*, 2020). Owing to the current global warming, the frequency and intensity of these events are increasing in many parts of the world (Hirabayashi *et al.*, 2008; Trenberth, 2006). One of the most important climate signals at global scale that might exacerbate these impacts is El Niño–Southern Oscillation (ENSO) (Wang *et al.*, 1999; Wang and Fiedler, 2006). With a variability that oscillates between 2 and 8 years (e.g., Moy *et al.*, 2002; D'Arrigo *et al.*, 2005), ENSO events substantially modify the mean ocean temperatures, tropospheric winds and atmospheric moisture transport, thus significantly changing ocean and surface air temperatures and hence the magnitude and distribution of rainfall in large regions around the world (Diaz *et al.*, 2001; Chiew and McMahon, 2002), among other effects.

Previous studies have shown that, on average, during a positive ENSO episode (i.e., El Niño) there is less rainfall and higher temperatures over the northern part of South America, while during a negative episode (i.e., La Niña), temperatures are lower and the amount of rain is higher in that region (Souza and Ambrizzi, 2002; Grimm and Tedeschi, 2009; Cai *et al.*, 2020). Therefore, ENSO events are related to a remarkable increase or decrease in the number and severity of floods and/or droughts, depending on the affected region as well as on the ENSO phase and onset characteristics (Capotondi *et al.*, 2015; Navarro-Monterroza *et al.*, 2019). Also the phase of the Pacific Decadal Oscillation (PDO) affects the periodicity of ENSO events (Ceron *et al.*, 2020; Canchala *et al.*, 2020c).

In South America, one of the most impacted countries by the ENSO episodes is Colombia (e.g., Poveda *et al.*, 2010; Hoyos *et al.*, 2013; Pinilla Herrera and Pinzón Correa, 2016; Ceron *et al.*, 2020; Contreras *et al.*, 2020). The relatively large surface area of the country (>1.1 million of km²), its complex topography with the high Andean Mountains separating the Pacific coast from the interior, the incursion of the Amazon rainforest in the southeastern side of the country and the long coastline (>3,000 km), which extends along parts of the colder eastern Pacific Ocean and the warmer Caribbean Sea, contribute to the existence of several climate zones and types. This diversity adds more complexity to forecasting regional impacts induced by ENSO episodes (Canchala *et al.*, 2020a; 2020b; Cerón *et al.*, 2021b).

Until now the main indicators of potential ENSO-induced seasonal and subseasonal climate variations in Colombia were oceanic ENSO indices based on sea surface temperature anomalies (SSTA)—such as the ENSO 3.4, ENSO 4, ENSO 1+2, ENSO 3, the Oceanic Niño Index and derived indexes such as those of Takahashi *et al.* (2011); Sullivan *et al.* (2016)—or atmospheric indicators such as sea level pressure anomalies (SLPA) in the Pacific basin, for example, the Southern Oscillation Index (e.g., Hanley *et al.*, 2003; Córdoba-Machado *et al.*, 2015). Despite some studies have been rather successful in capturing ENSO effects on rainfall with some anticipation in southwestern Colombia (Navarro-Monterroza *et al.*, 2019; Canchala *et al.*, 2020a; 2020c; Cerón *et al.*, 2021b), these indexes are calculated considering large regions in central and eastern Pacific Ocean and only consider one variable (SSTA or SLPA). As a consequence they do not properly account for local singularities, such as the effect of mountains in wind and cloud patterns or the nonlinear SST–convection relation (Fang and Mu, 2018; Xie *et al.*, 2020), which may have a strong impact in the distribution of rainfall, wind and surface air temperature.

In a try to overcome some of the above constraints and to get a more accurate prediction of the impact of ENSO events over Colombia, the Maritime General Directorate of Colombia (Dimar), thanks to the support provided by the Governorate of Magdalena department, has driven the development of a regionalized climate index. Benefiting from the existence of daily time series of in situ measurements of surface water temperature, air surface temperature and rain from 1961 in Tumaco, a city located in the southwestern Pacific coast of Colombia (near the border with Ecuador, see star in Figure 1), Rodríguez-Rubio (2013) developed a multivariate climate index based on a principal component analysis (PCA) of the above three variables. Results yielded two dominant components of variability: one that reproduced the inter-annual variability of ENSO (spectral peak at 2–8 years) that accounted for more than 50% of the total variability, and another one that contained two interdecadal modes of 8–16 year (PDO) and 20–30 year that accounted for 34% of the total variability. Based on these properties, the first mode was used to construct the Tumaco multivariate index (TMI, referred as IMT in Spanish), which is highly correlated (>0.6) with traditional ENSO indexes such as the ENSO 3, ENSO 1+2 and ENSO 3.4 (Rodríguez-Rubio, 2013). One important drawback of the TMI is that

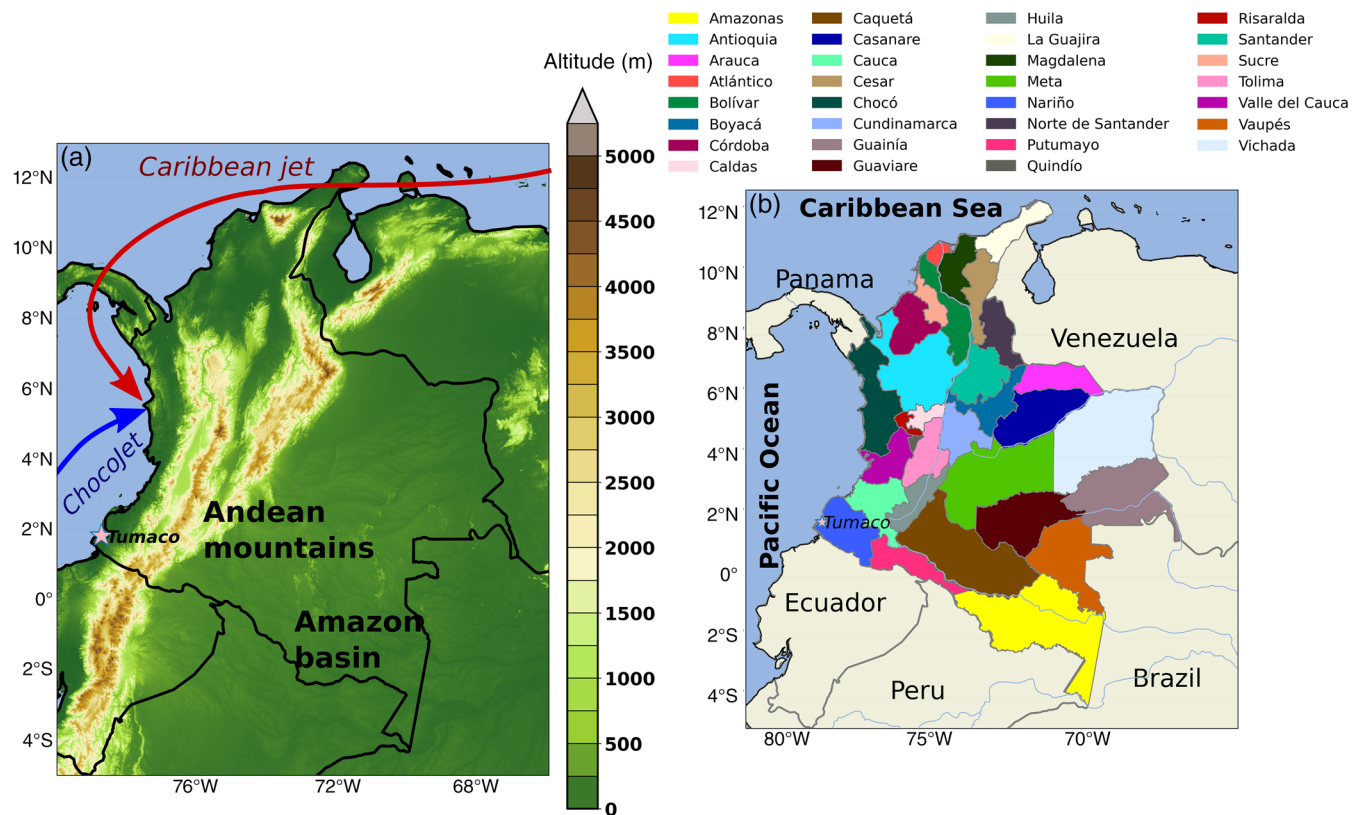


FIGURE 1 Maps showing: (a) elevation, rivers and main features of Colombia; and (b) the administrative departments of mainland Colombia (the department of San Andrés and Providencia Islands located further north is not shown, other are written in the legend). ChocoJet and Caribbean jet refer to Chocó low-level jet (blue arrow) and to Caribbean low-level jet (red arrow), respectively. Altitude is based on ASTER Global Digital Elevation Model (GDEM) version 3 (ASTGTM), obtained from NASA at: <https://search.earthdata.nasa.gov/>. The position of the city of Tumaco is denoted by a black star in both maps [Colour figure can be viewed at wileyonlinelibrary.com]

the highest correlation between the TMI and ENSO indices occurs with a lag of 1–2 months, with the TMI lagging behind ENSO indexes. This delayed response of TMI limits its usefulness and predictability skills. However, the availability of a reconstructed time series of sea level in Tumaco (with data since 1961) allows the inclusion of the sea level as an additional variable in the TMI construction.

In this article, we first analyse how the properties of the TMI are modified when sea level data is added in its construction. After that, the modified TMI, hereinafter named as TMI4, is tested for selected positive and negative ENSO episodes in which we explore the use of the TMI4 to anticipate the occurrence of rain anomalies over mainland Colombia. To start the validation of TMI4 in an operational environment, the computation of TMI4 has been semi-automatized and a visual interface has been implemented. This tool is currently only available to members of the operational oceanography team at Centro de Investigaciones Oceanográficas e Hidrográficas del Pacífico (Dimar-CCCP), and for completeness is sketched out in Appendix.

The article is distributed as follows: in section 2 the area of study is introduced; in section 3 data and methods are described; a thorough comparison between the TMI and the TMI4 is included in section 4, which includes a detailed analysis of observed sea level; the connection between TMI4 and rainfall for extreme ENSO events is evaluated in section 5; finally, section 6 includes a summary of the main conclusions and an outline of future challenges to continue enhancing the TMI4 forecasting capabilities.

2 | AREA OF STUDY

Colombian waters can be divided into those that belong to the Pacific basin and those that are part of the Caribbean basin. Both basins are separated by the Andean Mountains chain, with altitudes that can surpass 5,000 m (Figure 1a). Observations used to construct TMI and TMI4 are routinely taken at Tumaco, in the Nariño Department, within the southern Pacific Colombian region (purple star in Figure 1). Tumaco is located in the equatorial strip, in an area of low-pressure systems where

trade winds from both hemispheres converge. This interaction of air masses with different temperature and humidity properties favours the formation of a band of clouds by convection, which results in the presence of relatively weak winds and a large amount of rain near the coast that exceeds 3,000 mm per year (Poveda *et al.*, 2002). The climate there is classified as tropical, rainy, and isothermal in the Köppen System, which suggests the existence of rain throughout the year. The relative humidity oscillates between 85 and 95%, and the surface air temperature for the coldest and the warmest months takes values between 23 and 28°C, respectively. It is remarkable the presence of the Chocó low-level jet (ChocoJet; Figure 1a), which brings southwestern relatively cold winds that carry a large amount of moisture from the Pacific Ocean following a seasonal cycle. The ChocoJet is strong from September to November with mean velocities of 5–7 m·s⁻¹ and maximum velocities over 10 m·s⁻¹, and weakens from March to May (Poveda and Mesa, 1999; Rueda *et al.*, 2007; Durán-Quesada *et al.*, 2017; Yepes *et al.*, 2019; Ceron *et al.*, 2020). The kernel of the ChocoJet is located at 5°N and 80°W, at a height of 925 hPa (Arias *et al.*, 2015). Its strength is modulated by the air surface temperature gradient between the ENSO 1+2 region and waters off western Colombia (Poveda and Mesa, 2000), and by the sea surface temperature gradient between the Pacific and the Caribbean basins (Cerón *et al.*, 2021a).

In contrast to the Pacific region of Colombia, in the Caribbean region there is a strong seasonality in rainfall partly driven by the latitudinal migration of the Inter-tropical Convergence Zone (ITCZ) and the American Monsoon which modulate the easterly winds and depict two main seasons: the dry season, that extends from December to April; and the wet season, that extends from August to November (Amador, 1998; Poveda and Mesa, 1999; Esquivel *et al.*, 2018; Urrea *et al.*, 2019), although there are transition months (e.g., the mid-summer drought, in July). During the dry season the dominant trade winds flow from Northeast due to the northward location of ITCZ, while during the wet season the trade winds weaken since the ITCZ moves southward (Andrade, 1993; Martinez *et al.*, 2019). A relevant feature is the Caribbean low-level jet (locally known as “San Andrés,” hereinafter simply CLLJ), which is a surface branch of trade winds that brings relatively warm air from the East at a latitude between 12°N and 14°N (Poveda and Mesa, 1999; Martis *et al.*, 2002; Poveda *et al.*, 2002; Andrade and Barton, 2009). After crossing the Isthmus of Panama, this jet turns southeastward to reinforce the ChocoJet off the Pacific coast of Colombia (Figure 1a). The CLLJ has a semi-annual cycle, with two maxima in summer and winter, and two minima in fall and spring (Wang, 2007; Orfila *et al.*, 2021), in good

accordance with the semi-annual cycle of SLP and SST gradients in the region (Wang, 2007). Similarly to ChocoJet, the kernel of the CLLJ is located at a height of 925 hPa and might reach a height over 700 hPa (Amador, 2008). The strength of the CLLJ is associated with the position of the North Atlantic Subtropical High, which varies with the North Atlantic Oscillation (Wang, 2007; Amador, 2008). Overall the relative minimum rainfall in the area takes places in July, when the CLLJ is strongest.

Both the eastern Pacific and the eastern Pacific-Caribbean Sea interbasin surface air and SST gradients modulate the interaction between the close to the surface colder and humid ChocoJet convergent wind and the warmer high-level eastern trade winds (including CLLJ). Together with the orographic lift induced by the presence of the Andean Mountains, they contribute to form a large amount of mesoscale activity, and consequently rain, in western and central areas of Colombia (Poveda and Mesa, 2000; Cerón *et al.*, 2021a). Instrumental records indicate that values of annual accumulated rainfall can reach values between 8,000 and 13,000 mm in some specific areas (Poveda and Mesa, 2000), being one of the rainiest regions on the Earth.

Regarding the known impacts of ENSO events on Colombia, the main affected regions are the Pacific and Caribbean ones, although much weaker in the latter (Handoh *et al.*, 2006; Okumura and Xie, 2006; Wang and Fiedler, 2006). The interior part of Colombia is less sensitive since the high Andean Mountains partly act as a barrier, thus reducing the impact of wind and temperature anomalies in coastal areas by blocking and/or drying airmasses by orographic lift (Puertas and Carvajal, 2008; Poveda *et al.*, 2010). Indeed the Amazon basin is characterized by its own low-level jets that form in the Atlantic side of South America (Espinoza *et al.*, 2020). It is known that during a positive ENSO event (El Niño) the amount of rain decreases and the mean temperatures increase over a large part of the Colombian Pacific region due to the weakening of the ChocoJet, as well as over the Caribbean region and in the centre-north of Colombia thus favouring the development of droughts. In contrast, during negative ENSO events (La Niña) the mean amount of rain increases and temperatures decrease due to the strengthening of the ChocoJet thus favouring the occurrence of floods (Poveda *et al.*, 2010; Serna *et al.*, 2018). Interestingly, the CLLJ has an opposite relationship with ENSO depending on the season. During winter, a weak (strong) CLLJ is associated to positive (negative) SST anomalies in the tropical Pacific, while in summer a strong (weak) CLLJ corresponds to positive (negative) SST anomalies in the tropical Pacific (Wang, 2007). Alternatively, in the Amazon basin (southeastern side of Colombia) the relationship between ENSO and extreme

rainfall events appears to be strongly influenced by the Madden–Julian Oscillation phase (Shimizu *et al.*, 2017). To conclude this section, we note that the magnitude of the threats will depend on several aspects such as the phase, magnitude, flavour or onset of the ENSO event (whether it occurs in the eastern Pacific–El Niño/La Niña Canonical, or in the central Pacific–El Niño/La Niña Modoki), as well as on the season that the ENSO impacts on Colombia (L'Heureux *et al.*, 2017; Serna *et al.*, 2018; Navarro-Monterroza *et al.*, 2019).

3 | DATA AND METHODS

In this section, first the input dataset employed to construct TMI and TMI4 indices are described. After that, complementary gridded dataset of rain, wind, sea surface temperature and time series of ENSO indices are also

described. These complementary data are used to explore the relationship between ENSO indices, and TMI and TMI4 in section 4, as well as between TMI4 and rainfall over mainland Colombia in section 5. Finally, we remind the methodology followed to construct the TMI and how is here extended to construct TMI4 with the addition of sea level data.

3.1 | TMI4 input data

Time series of monthly sea surface temperature (see SST anomalies in Figure 2a) and atmospheric data (surface air temperature [AT] and accumulated rain, anomalies are shown in Figure 2b,c, respectively) are registered in a coastal station from “Centro de Investigaciones Oceanográficas e Hidrográficas del Pacífico-CCCP,” in Tumaco (purple star in Figure 1). Despite there are other

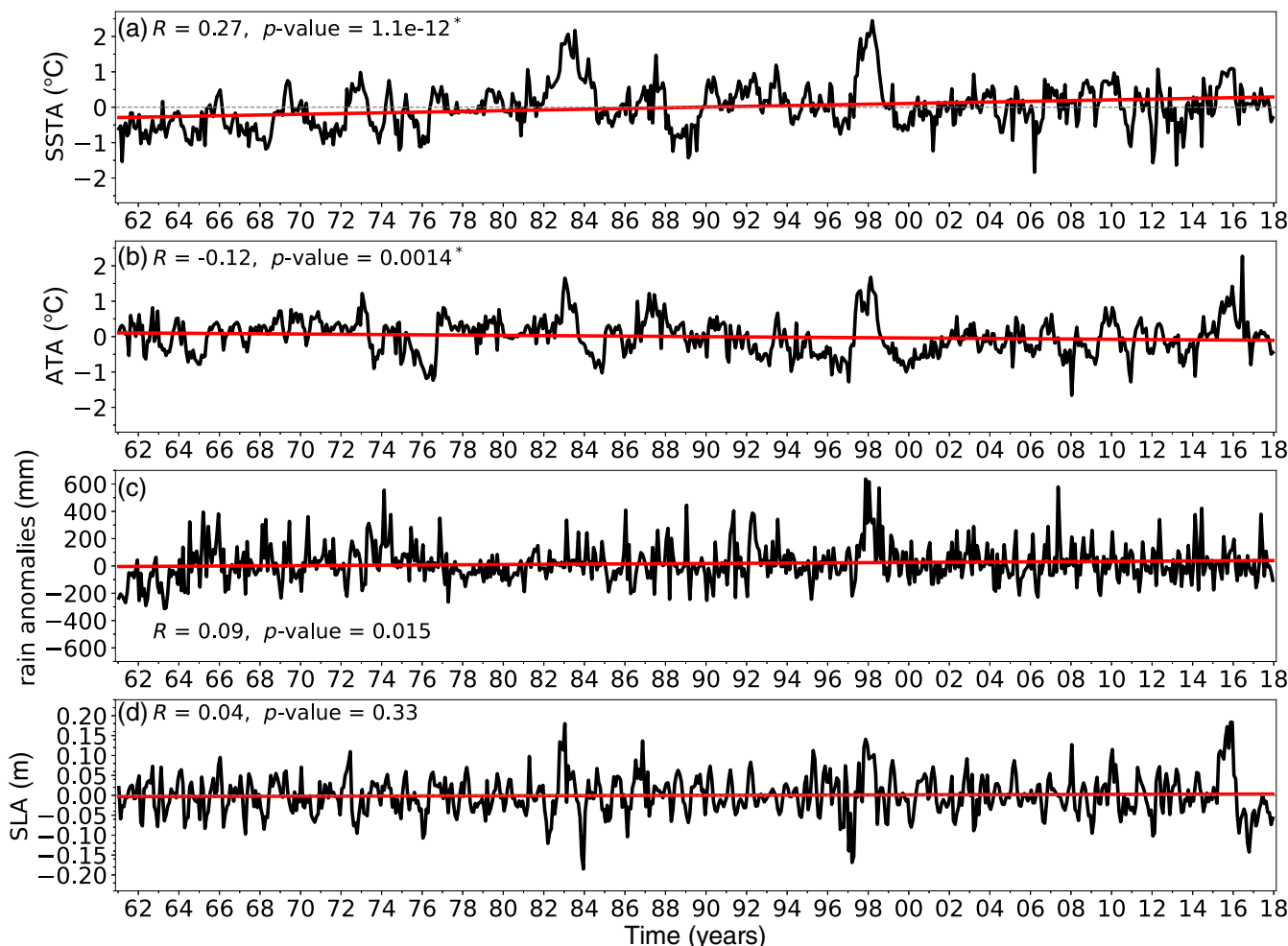


FIGURE 2 Monthly time series of the TMI input data measured at Tumaco: (a) sea surface temperature anomalies (SSTA, in °C), (b) surface air temperature anomalies (ATA, in °C), (c) monthly accumulated rain anomalies (in mm) and (d) sea level anomaly (SLA, in m). Linear trends are denoted with red solid lines at each panel. To compute the anomalies the mean value has been subtracted to each time series (zero is depicted by a thin horizontal grey dashed line). *P*-values are estimated from a 2-tailed *t*-Student distribution, and significant values at 95% are marked with an asterisk [Colour figure can be viewed at [wileyonlinelibrary.com](https://onlinelibrary.wiley.com)]

stations in neighbouring departments (but with intermittent measurements since the 1990s), the longest and most complete monthly time series in the Pacific basin, from 1961 until recently, are based in Tumaco. Therefore these time series were selected to construct the TMI index (Rodríguez-Rubio, 2013). For the purpose of this study we will cover the years 1961–2017 (both years included), but routinely daily measurements are still being taken.

Several statistical methods were applied to preserve the quality and homogeneity of time series, including the standard normal homogeneity test (e.g., Thom, 1966; Brockwell and Davis, 1993), seasonal decomposition (Wei, 2006), the use of geospatial models (Barón-Leguizamón, 2003) and the validation with available satellite measurements. When possible, geospatial models and/or satellite data were used to fill gaps in precipitation and air temperature time series. As seen in Figure 2a–c, there are positive and negative linear trends in SST and AT anomalies significant at 95%. However, these trends should be taken with caution, since they show a very high temporal variability and the variance explained by the model ($R^2 < 0.1$ for all cases) is very low.

The main novelty of this work is that we include in the construction of TMI4 monthly sea level data (see sea level anomalies [SLA] in Figure 2d) measured at Tumaco (78.73027°W, 1.81930°N). Time series of hourly sea level was retrieved from the University of Hawaii Sea Level Center (UHSLC), <https://uhslc.soest.hawaii.edu/>. This repository is part of the Joint Archive for Sea Level (JASL), which includes a documented preliminary quality control (Caldwell and Merrifield, 2015). Outliers were exhaustively evaluated and gaps were filled with the tidal components obtained from an harmonic analysis performed with UTide software (Codiga, 2011), and with the annual and semi-annual sea level components derived from a Fourier decomposition (e.g., Marcos and Tsimplis, 2007).

3.2 | Gridded sea level and geostrophic velocities

Gridded sea level and ocean geostrophic velocity anomalies derived from altimetric measurements are used in section 4 to identify the equatorial Kelvin waves. Among the available products, we use the interpolated daily (derived from the original weekly fields) two-satellite delayed time series formerly distributed by AVISO+, and now available at Copernicus Climate Change Service (<https://climate.copernicus.eu/>). This product has a global coverage from 1993, and a spatial resolution of $0.25^\circ \times 0.25^\circ$. The correlation map between monthly SLA measured at Tumaco (Figure 2d) and satellite-based SLA is shown in Figure 3a. The spatial distribution of the largest correlations, with values close to 0.5, form a tongue-like pattern around the

equatorial strip from the northwestern South American coasts towards the central Pacific. As seen, an opposite tongue-like pattern of negative correlations that reach values of about -0.5 are found in the western equatorial Pacific and extends towards the central Pacific too. This pattern is consistent with the sea level pressure distribution in the Pacific basin (lower pressure in the western, higher pressure in the eastern) and shows that sea level measurements at Tumaco are representative of the surface ocean dynamics that takes place along the equatorial strip.

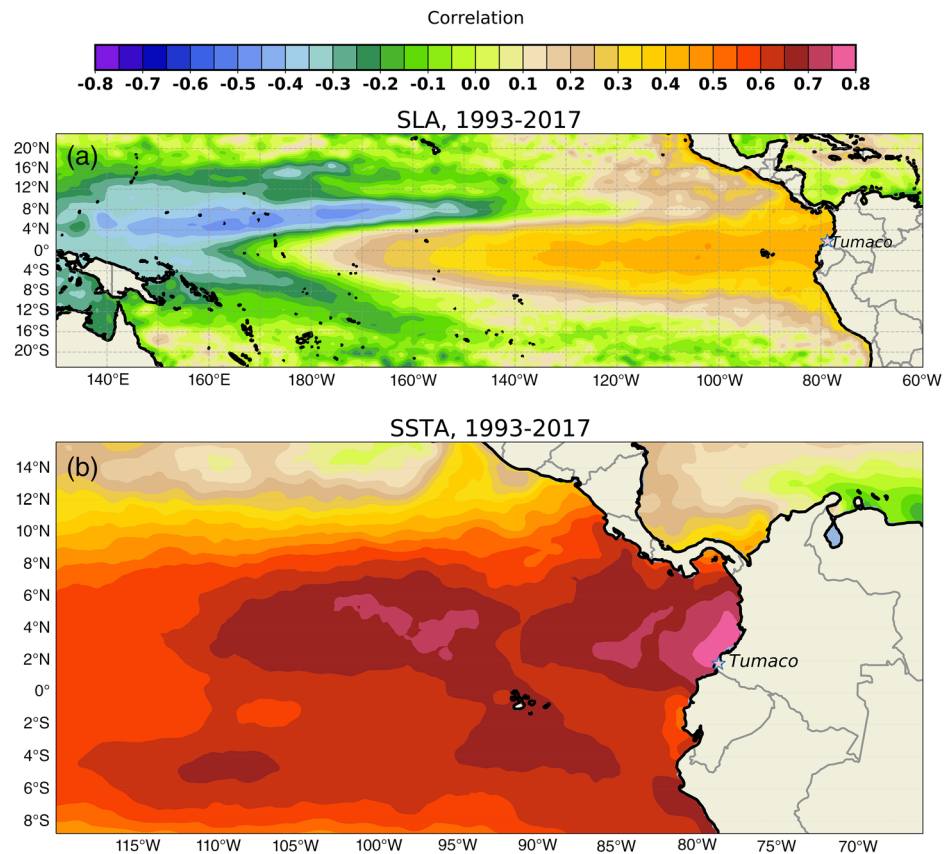
3.3 | Sea surface temperature

To characterize ENSO events, we have used gridded SST data from on board, satellite-based infrared sensors. This product has been created by the group for high-resolution sea surface temperature (GHRSSST). We have selected the NOAA optimum interpolation $0.25^\circ \times 0.25^\circ$ daily SST analysis from the National Centers for Environmental Information (NCEI), also available at the Physical Oceanography Distributed Active Archive Center (PODAAC, known as the GHRSSST Level 4 AVHRR_OI Global Blended SST analysis GDS version 2). Data are available since September 1981 and gridded SST fields are obtained from optimally interpolating and extrapolating observations measured by the advanced very high-resolution radiometer (AVHRR) sensors. This dataset includes information from in situ platforms such as ships and buoys (Banzon *et al.*, 2016). Data are accessible at https://podaac.jpl.nasa.gov/dataset/AVHRR_OI-NCEI-L4-GLOB-v2.0. Figure 3b shows how this product correlates with monthly mean measurements taken at Tumaco station (Figure 2a). As seen, SSTA variability at Tumaco is in good agreement with SSTA variations around the Pacific Colombian coast, with correlations of 0.7 and larger.

3.4 | ENSO indices

Several ENSO oceanic indices based on SST anomalies are widely employed to regionally monitor the evolution of ENSO. Among the most traditional are ENSO 1+2, ENSO 3, ENSO 3.4 and ENSO 4 indices, which cover the tropical eastern and/or central Pacific Ocean. Monthly indices since 1948 are available from NOAA Physical Sciences Laboratory, <https://www.psl.noaa.gov/data/> (Trenberth and National Center for Atmospheric Research Staff, 2020). Over the last few years other indices have been derived from the latter to better capture ENSO flavours: mainly the central Pacific (El Niño Modoki) and the eastern Pacific (El Niño Canonical) events. Here we use those of Takahashi *et al.* (2011), where $C \simeq 1.7$ ENSO 4–0.1 ENSO 1+2, and $E \simeq$ ENSO

FIGURE 3 (a) Map showing the Pearson correlation between monthly satellite-based sea level anomalies (SLA) and the SLA measured at Tumaco used to construct the TMI4 (Figure 2d). Correlations cover the period 1993–2017 and the tropical Pacific Ocean. (b) Same as (a) but for satellite-based sea surface temperature anomalies (SSTA) and SSTA observations at Tumaco (Figure 2a). The location of Tumaco is denoted by a star in both maps. Note that the map is reduced for SSTA correlations to facilitate the observation of the larger spatial variations [Colour figure can be viewed at wileyonlinelibrary.com]



1+2–0.5 ENSO 4, are constructed to better capture the central and eastern Pacific Niños, respectively; and those of Sullivan *et al.* (2016): CP = ENSO 4–0.5 ENSO 3, EP = ENSO 3–0.5 ENSO 4, and Mixed = EP + CP, where CP and EP also refer to distinguishable central and eastern Pacific El Niño, while Mixed collects the undefined events.

3.5 | Surface wind

Gridded surface wind data is obtained from Remote Sensing Systems (RSS). Cross-Calibrated Multi-Platform (CCMP) Version 2.0 wind vectors are constructed through the combination of satellite, moored buoy, and model wind data. The Version 2.0 merges Version-7 RSS radiometer wind speeds, QuikSCAT and ASCAT scatterometer wind vectors, moored buoy wind data, and ERA-Interim model wind fields using a Variational Analysis Method to produce 6-hourly maps at a spatial resolution of $0.25^\circ \times 0.25^\circ$. Data are available from 1988 and freely downloadable at <http://www.remss.com/measurements/ccmp/>.

3.6 | Rainfall gridded data

State-of-the-art high resolution gridded rainfall data with long temporal coverage (at least 30 years) and mostly

based on observations are used in section 5 to analyse how the TMI relates to rainfall anomalies during ENSO events.

3.7 | CHIRPS

Climate Hazards Group InfraRed Precipitation with Station data (CHIRPS) is a quasi-global rainfall data set, with daily records of total rainfall available from 1981 to near-present. Its coverage is global from 50°S to 50°N , and contains the University of California-Santa Barbara climatology (CHPclim), 0.05° satellite imagery, and in situ gauge data to create gridded rainfall time series with a spatial resolution of $0.05^\circ \times 0.05^\circ$ (Funk *et al.*, 2015). Data are publicly accessible at: <https://data.chc.ucsb.edu/products/CHIRPS-2.0/>.

3.8 | PERSIANN-CDR

Also PERSIANN-CDR (Precipitation Estimation from Remotely Sensed Information using Artificial Neural Networks), available at <https://data.nodc.noaa.gov/cgi-bin/iso?id=gov.noaa.ncdc:C00854>, is used in this work. This dataset provides daily total rainfall at a spatial resolution of $0.25^\circ \times 0.25^\circ$, with a quasi-global coverage (from 60°S to 60°S) since 1983. The information has been

optimally integrated through artificial neural networks by the Center for Hydrometeorology and Remote Sensing (CHRS) at the University of California-Irvine (Nguyen *et al.*, 2019).

3.9 | Methodology for TMI4 construction

Similarly to the method described by Rodríguez-Rubio (2013) to construct the Tumaco multivariate index (TMI), the new index, TMI4, is constructed following four basic steps (see a sketch in Figure 4). First, time series of SST, air temperature (AT), rain and sea level (SL) at Tumaco were processed and quality controlled as explained in section 3.1 and monthly values were calculated. Second, anomalies of all four variables were computed through a standardization process in which the corresponding climatological monthly mean (the median for the particular case of the rain) for a base period of 30 year subtracted to each variable. Then, each of the resulting time series were normalized by dividing them by their standard deviation for the same base period. We have tested two base periods (climatologies): 1971–2000 and 1986–2015. These two periods are selected to test the robustness of TMI/TMI4 since they include ENSO events of different characteristics (magnitude and period). Once time series have been standardized, a Principal Component Analysis (PCA) is performed over the anomalies (Storch and Zwiers, 1999; Emery and Thomson, 2001). It yields four components, the same as the number of input variables. Among these components, the one that explains most variance (>40%) is selected since it predominantly represents the interannual variability associated with ENSO, as previously shown by Rodríguez-Rubio (2013). Finally, a 3-month moving average is applied over the selected principal component to smooth the extremes, as part of the method followed by Kousky and Higgins (2007)

to classify the values of ENSO indices. The resulting time series once sea level data is included is called TMI4, with values within the range of -5 and 5 , and susceptible of being classified according to its persistence and intensity, analogously to other ENSO indices. A more detailed description of the operational implementation of TMI4 and its interpretation is provided in Appendix. The PCA analysis if performed with the Python library *eofs*, freely accessible at: <https://ajdawson.github.io/eofs/latest/>.

3.10 | Wavelet analysis

In order to characterize interannual variability of TMI4 we perform a wavelet analysis. Following Torrence and Compo (1998); Canchala *et al.* (2020b), the mother wavelet selected is of type “Morlet,” which decomposes the signal in a space of time and frequency through a complex exponential modulated by a Gaussian window. The obtained spectrum has been rectified following the method of Liu *et al.* (2007). Wavelets are computed with the Python library *pycwt*, freely accessible at: <https://pycwt.readthedocs.io/en/latest/#>.

3.11 | Prewhitening of a time series

In some analyses we will be interested in minimizing the autocorrelation of time series before computing their correlation. It allows to interpret the magnitude of the correlation without undesired deterministic signals, which can yield a wrong impression of the cause–effect relationship between any two given variables (Orfila *et al.*, 2005). To isolate the stochastic component (or residual) in a time series we do a prewhitening by applying the seasonal autoregressive integrated moving average (SARIMA)

Steps to construct the new Tumaco Multivariate Index (TMI4)

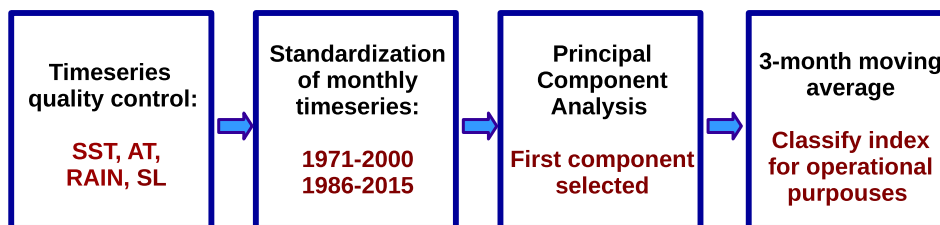


FIGURE 4 Flow diagram that shows the steps followed to construct the new Tumaco multivariate index (TMI4). First, time series of sea surface temperature (SST), air temperature (AT), rain and sea level (SL) measured at Tumaco are processed and quality controlled. The second step is the standardization of monthly time series with respect to a reference climatology of 30 years (e.g., 1971–2000 or 1986–2015). Once time series are standardized a principal component analysis (PCA) is performed over the input time series, from which the first component is taken. To conclude, the selected principal component is smoothed with a 3-month moving average and then classified according to an operational table further described in Appendix [Colour figure can be viewed at wileyonlinelibrary.com]

model (e.g., Valipour, 2015). SARIMA allows to subtract periodic and stationary signals such as the trend and the seasonal cycle, and smooths regression errors according to a set of coefficients that can be specified. It is implemented with the `pmdarima` library, available for Python language at <https://alkaline-ml.com/pmdarima/about.html>. The goodness of fit between the different obtained models is estimated with the Akaike information criterion (Akaike, 1974).

4 | PERFORMANCE OF TMI AND TMI4: COMPARISON WITH ENSO INDICES

In this section TMI and TMI4 (i.e., the 3-month moving average of the first principal component of Tumaco-based input observations, PC_1 , obtained without and with the addition of sea level data, respectively), are compared for two different base periods, which are defined as the period selected for climate data standardization: 1971–2000 and 1986–2015, respectively. As mentioned above, these two periods are selected to test the robustness of TMI/TMI4 since they include different ENSO events. To this end, the interannual variability of TMI and TMI4 is first characterized by means of a wavelet analysis. After that, correlations between ENSO oceanic indices and TMI and TMI4 time series will be compared for two different cases: when original signals are correlated, and when only the residual (stochastic) component of signals are correlated (section 3.9). Moreover, the new information provided by sea level data on the onset of ENSO is analysed in detail. Based on these results, the most suitable index is selected for further analysis.

Figure 5 shows TMI and TMI4 time series (grey solid line) for base periods 1971–2000 and 1986–2015 (Figure 5a,b and Figure 5c,d, respectively). Unsurprisingly, due to the smaller number of variables used to construct the TMI the variance of the first PC_1 (solid black line) is larger than for TMI4 (~9% more, with small differences for studied base periods), with larger weights (see percentages inside panels) for SST and AT than for accumulated rain. Regarding the time series of TMI4, sea level contributes to the PC_1 about 26 and 23% for base periods 1971–2000 and 1986–2015, respectively. As seen, the contribution of sea level is larger than the contribution of rain, thus indicating that sea level adds new statistical variability to the TMI4 not previously included in the TMI. Moreover, one notable result is that ENSO events show larger peaks for TMI4 (e.g., those of 1983 and 2015 associated with strong El Niño events) than for TMI (compare Figure 5a,c against Figure 5b,d).

In order to analyse how the above differences in TMI and TMI4 properties are reflected in its interannual variability we proceed to perform a wavelet analysis for the same study cases shown in Figure 5. Time series of energy density of TMI and TMI4 are shown in Figure 6e and Figure 6c,g with shading colour, respectively. Patterns are rather similar except for two details that are shown more clearly in the global spectrum (Figure 6b,d,f, h): a secondary peak more energetic at a period of 2.3 year (Figure 6b,f) for TMI than for TMI4, which is likely associated with the quasi-biennial oscillation as suggested by Rodríguez-Rubio (2013); and a secondary peak more energetic at 1.5 year for TMI4 than for TMI (Figure 6d,h). Indeed the latter peak at 1.5 year also appears, although less energetic, for TMI (Figure 6b,f). Another difference to note is the bandwidth of the interannual energy density associated with ENSO events in TMI and TMI4, which is sharper and better defined for TMI with a clear peak at a period of 4.9 year (Figure 6b,f), than for TMI4 that shows several peaks between periods of 2.8 and 4.9 year. One reason that explains this difference is the larger relevance in terms of energy of El Niño 1998 event in the time series of TMI than for time series of TMI4 (Figure 5). This view is supported by the larger peak for El Niño 2015 in the time series of energy density variance for a period between 2 and 8 year for TMI than for TMI4 (solid blue line in Figure 6a,e and Figure 6c,g, respectively). ENSO events have a barely predictable interannual variability that oscillates between 2 and 8 year (e.g., Moy *et al.*, 2002; D'Arrigo *et al.*, 2005), therefore the broader bandwidth shown for TMI4 (Figure 5b,d) is more realistic as it covers ENSO events with different characteristics. Regarding those differences caused by the base period employed to perform the standardization, we would like to mention two features: the better defined peak at 4.9 year for the base period 1971–2000 than for 1986–2015 (Figure 6b,f, respectively), and the largest interannual peaks with respect to the secondary peak at 1.5 year for the base period of 1986–2015 than for 1971–2000 (Figure 6h and Figure 6d, respectively).

The relationship between TMI/TMI4 and selected regional and derived ENSO oceanic indices based on SST (described in section 3.4) is evident in terms of the Pearson correlation (Table 1). As seen, correlations between TMI/TMI4 and ENSO indices give maximum values over 0.7 for the closest indices (ENSO 3, ENSO 1+2 and EP) and for all study cases. The correlation drops to about 0.65 for ENSO 3.4 and E, and to around 0.5 for ENSO 4 and C, which is the farthest from Tumaco. The lowest correlations are found for CP (about 0.2), which merges ENSO 4 and ENSO 3 signals. Thus, correlations tend to degrade as the spatial distance between Tumaco and the regions in which indices are computed increases. For all

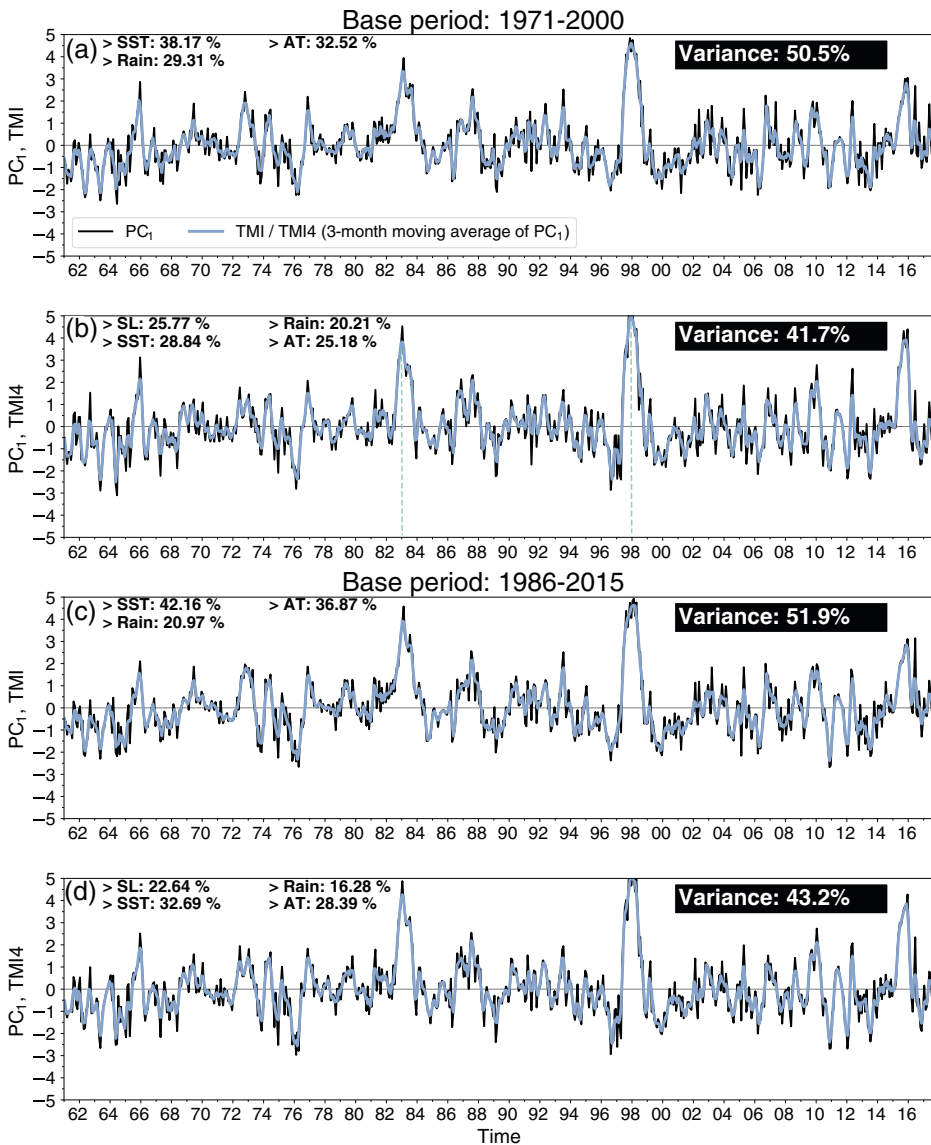


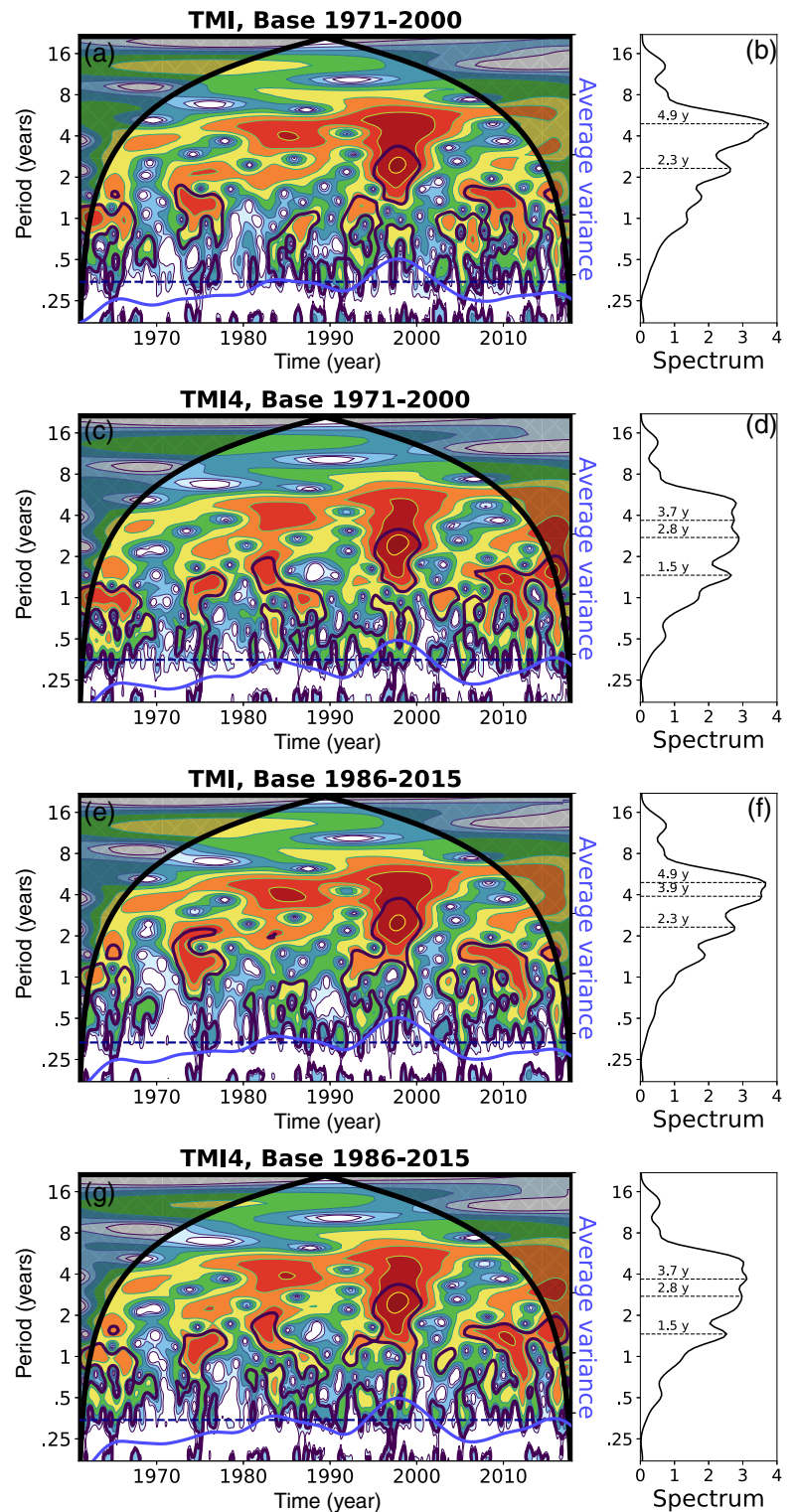
FIGURE 5 Time series of TMI (a-c), and TMI4 (b-d). TMI and TMI4 are shown for two different base periods: (a, b) 1971–2000 and (c, d) 1986–2015. The black line denotes the first component (the one that explains most variance, PC_1) obtained from the PCA analysis (section 3.7). The grey line is the 3-month average of PC_1 , which is as the indexes are defined (Rodríguez-Rubio, 2013). Variables used in each case and their weight in the construction of TMI and TMI4, as well as the explained variance by the PC_1 are shown in the top-left and in the top-right of each panel, respectively [Colour figure can be viewed at wileyonlinelibrary.com]

study cases lag times at which maximum correlations are obtained are negative (1 or 2 months), except for TMI4 (Table 1), which yields the highest correlation at lag 0 with ENSO 3 (1971–2000), E (1971–2000) and EP (both base periods). These results suggest that the TMI responds with certain delay with respect to regional ENSO indices. To deepen more in the contribution of sea level, correlations are calculated again after subtracting the autocorrelation (Table 2, note how the autocorrelations of residual signals quickly drop to 0 at 1 month lag for all cases in Figure S1, Supporting Information), which includes the removal of the trend and the seasonal component after applying the SARIMA model described in section 3.9.

Unsurprisingly the maximum correlations drop, now reaching values between 0.1 and 0.21 (all of them significant at 99% according to a *t*-Student 2-tailed distribution). Maximum correlations are larger for the base period

1986–2015 and also degrade with the distance to regions where ENSO indices are computed with respect to Tumaco. Regarding lag time, now TMI and TMI4 vary simultaneously or even lead the variability for 1 month against ENSO 1+2 and E, and lead for 1 month against the ENSO 3 and EP for all cases. For the farthest indices the delay is reduced when sea level data is included, being now nonexistent (lag = 0) against ENSO 3.4 and mixed, and of only 1 month against ENSO 4 and C for the base period 1986–2015. Again, CP is weekly correlated with TMI/TMI4 indices. These results point out that one cause that may explain the delay of TMI/TMI4 with respect to ENSO indices (Table 1) is the contribution of the large autocorrelation in the signals, which is most likely because of the long SST memory. However, once the deterministic components have been subtracted, the relevance of including sea level data in the construction of the index is revealed. Thus, the values of time lags

FIGURE 6 Wavelet transform (a, c, e, g) and global spectrum (b, d, f, h) of time series of TMI and TMI4 shown in Figure 4: TMI (first and third rows) and TMI4 (second and fourth rows); and for two different base periods: 1971–2000 (first and second row), and 1986–2015 (third and fourth row). The blue line denotes the variance of the spectral energy density and the horizontal dashed line is the threshold that separates significant values at 95% (which are located above the line) from other. Periods at which peaks of energy are obtained are denoted in the right panels. Black contours in left panels depict those values significant at 95% [Colour figure can be viewed at wileyonlinelibrary.com]



found in Table 2 for residual components indicate that the inclusion of sea level into the TMI may help to anticipate the development of ENSO events in comparison with regional ENSO indices only based on SST data.

Interestingly, the sequence of time lags found in Table 2 for TMI4 responds reasonably well to travel time characteristics of equatorial Kelvin waves that often

develop during ENSO events. Equatorial Kelvin waves are mostly found in the equatorial band (between 2°S and 2°N of latitude), where Tumaco is located. Downwelling Kelvin waves formed during the onset of El Niño events transport warm waters from western to central and eastern Pacific regions, in which the thermocline is pushed down. They take between a few weeks and about

TABLE 1 Cross-correlation between TMI/TMI4 and selected ENSO indices: ENSO 1+2, ENSO 3, ENSO 3.4 and ENSO 4, and other indices more adapted to regionally identify central Pacific and eastern Pacific ENSO events such as those of Takahashi *et al.* (2011) (C, E) and Sullivan *et al.* (2016) (CP, EP, Mixed), which are described in section 3.4. Correlations are performed for case studies shown in Figure 5: TMI (3 variables) and TMI4 (4 variables) and for base periods 1971–2000, and 1986–2015

Index	ENSO								
	1+2	ENSO 3	ENSO 4	ENSO 3.4	C	E	CP	EP	Mixed
TMI (1971–2000)	0.756 (–1)	0.734 (–1)	0.474 (–2)	0.639 (–1)	0.421 (–2)	0.682 (–1)	0.225 (21)	0.732 (–1)	0.665 (–1)
TMI4 (1971–2000)	0.708 (–1)	0.730 (0)	0.466 (–1)	0.647 (–1)	0.416 (–1)	0.633 (0)	0.185 (21)	0.736 (0)	0.659 (–1)
TMI (1986–2015)	0.773 (–1)	0.765 (–1)	0.518 (–1)	0.676 (–1)	0.464 (–1)	0.685 (–1)	0.230 (20)	0.751 (–1)	0.704 (–1)
TMI4 (1986–2015)	0.739 (–1)	0.762 (–1)	0.509 (–1)	0.681 (–1)	0.457 (–1)	0.651 (–1)	0.199 (21)	0.755 (0)	0.698 (–1)

Note: The highest correlations (in absolute value) and their associated time lag are shown in each panel for all indices. Values provided are significant at 99% ($p < .01$), according to a t -Student 2-tailed distribution. Lag times are shown in parenthesis: Positive means that TMI indices lead and negative that TMI/TMI4 follow ENSO indices. At lag = 0 correlated signals are simultaneous, while at other lags time series are shifted several months. Unit of time lag is month.

TABLE 2 Same as Table 1 but for the residual components (denoted by the subscript r). The residual components have been computed as explained in section 3.9

Index	ENSO _r 1+2	ENSO _r 3	ENSO _r 4	ENSO _r 3.4	C _r	E _r	CP _r	EP _r	Mixed _r
TMI _r (1971–2000)	0.182 (0)	0.157 (1)	0.130 (9)	0.141 (–3)	0.135 (9)	0.181 (0)	0.106 (–27)	0.168 (1)	0.131 (–3)
TMI4 _r (1971–2000)	0.180 (1)	0.171 (1)	0.122 (9)	0.129 (0)	0.129 (9)	0.172 (1)	0.111 (–27)	0.184 (1)	0.136 (0)
TMI _r (1986–2015)	0.209 (0)	0.183 (1)	0.136 (–3)	0.158 (–3)	0.127 (–3)	0.198 (0)	0.101 (–27)	0.197 (1)	0.150 (–3)
TMI4 _r (1986–2015)	0.203 (0)	0.197 (1)	0.120 (–1)	0.142 (0)	0.118 (–1)	0.182 (0)	0.112 (–27)	0.212 (1)	0.161 (0)

2 months to cross the Equatorial Pacific up to reach the western coast of South America, depending on their origin (Delcroix *et al.*, 1991; Rydbeck *et al.*, 2019), where they can be transformed into coastal trapped waves when they reach the western American continent (Huthnance, 1978; Mysak, 1980). One subset of equatorial Kelvin waves are the intraseasonal (IS) Kelvin waves, with periods of about 30–90 days, that can be derived from sea level data (see their range of periods denoted by horizontal dashed lines in Figure 7). Their relevance for monitoring (sub)seasonal climate variations in the eastern Pacific has been recently discussed in detail by Rydbeck *et al.* (2019). If, as we hypothesize, information on equatorial Kelvin waves is incorporated into TMI4 through sea level data, the anticipation of 1 month by the residual component of TMI4 with respect to the residual part of ENSO 3 index (located in the central East Pacific) could explain the early imprint of the fast Kelvin waves ($\approx 2 \text{ m}\cdot\text{s}^{-1}$) on sea level at Tumaco, which effect takes more time (1–2 months later) to be observed in SST. To confirm this process, a wavelet analysis over the hourly

time series of sea level data measured at Tumaco is performed in Figure 7. As seen, strong signals (shading) with periods of around 30–90 days are often found around positive peaks of TMI4 (black solid line in Figure 7). These energetic signals are clearly distinguishable for El Niño events of 1983, 1998 and 2015, especially when the time series of the variance of energy density of sea level for periods between 30 and 90 days (green solid line in Figure 7) is imposed over TMI4. Note that peaks of energy density variance in years 1991/1992 and 2002/2003 do not have associated a peak in TMI4, likely because those weaker Niño events stopped their development before large SST anomalies occurred nearby Tumaco (e.g., Hackert *et al.*, 2007). Due to the proximity of Tumaco tide gauge to the coast, the existence of other signals can degrade the imprint left by equatorial Kelvin waves (e.g., the presence of coastal trapped-waves) in the time series here analysed. Finally, one unclear point that we address in the next subsection is to what extent local wind is affecting the energy density captured by the Tumaco sea level time series at intraseasonal scales.

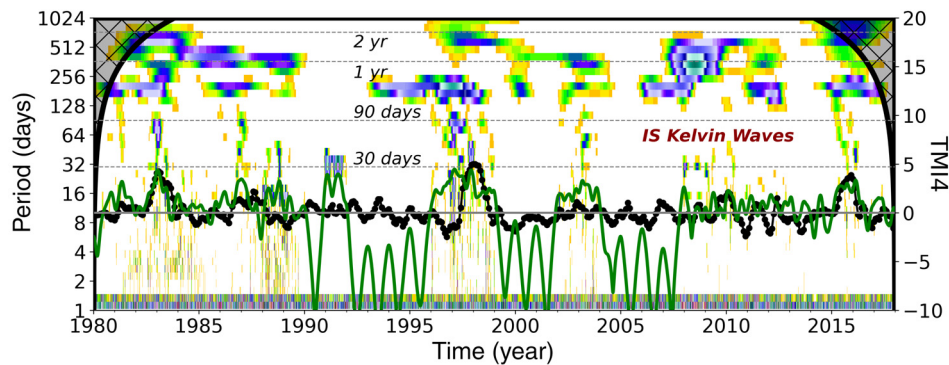


FIGURE 7 Wavelet of time series of sea level at Tumaco between years 1980 and 2017 (both included). Shading shows the energy density distribution for periods between 1 day and 2 year (left y-axis). Periods close to intraseasonal (IS) Pacific equatorial Kelvin waves are depicted by horizontal dashed lines at 30 and 90 days (Rydbeck *et al.*, 2019). Also periods of 1 and 2 year are depicted. Time series of TMI4 for base period 1986–2015 is shown by a black solid line (right y-axis). The energy density variance of sea level for periods between 30 and 90 days is shown by a green solid line [Colour figure can be viewed at wileyonlinelibrary.com]

4.1 | Exploring the influence of local wind on sea level at intraseasonal scales

Here we analyse the intraseasonality due to equatorial Kelvin waves and that due to local winds at Tumaco sea level time series. To this end, we follow the methodology of Boulanger and Menkes (1995), which allows to get not only the meridional structure of Kelvin waves on the equatorial Pacific from SLA, but also the wind-forcing component that exerts a direct influence on the generation of those equatorial Kelvin waves.

As described in detail in Boulanger and Menkes (1995), appendix) we have projected daily satellite-based SLA (described in section 3.2) onto long equatorial waves. This decomposition allows us to isolate the spatio-temporal variability of Kelvin waves along the equatorial strip as shown in Figure 8a. Downwelling (positive sea level anomalies that carry warmer waters towards the east and downward) and upwelling (negative sea level anomalies that try to restore neutral conditions bringing colder waters towards the west and upward) Kelvin waves are clearly depicted during strong El Niño events (Figure 8b). Consistently, a remarkable zonal propagation of sea level anomalies associated with the Kelvin mode exists during El Niño 1997/1998 and El Niño 2015/2016 (Figure S2).

Once equatorial Kelvin waves are characterized, we proceed to project the surface zonal wind anomalies onto the Kelvin mode as described in Boulanger and Menkes (1995), appendix 3) to obtain the wind-forcing component associated to Kelvin waves. Daily averaged cross-calibrated multi-platform (CCMP) winds described in section 3.5 are used in this analysis. Consistently, positive anomalies (weaker than usual easterlies) propagate from the western towards the eastern Pacific during the

onset of the strong El Niño events of 1997/1998 and 2015/2016 (Figure S3). If we now correlate local wind anomalies with the projected zonal wind-forcing associated to Kelvin waves, large correlations around the equatorial strip are found (above 0.9), which quickly vanish poleward off the equatorial band. Interestingly, these correlations degrade faster along the Pacific Colombian coast where values are below 0.4 (Figure 9a). This result suggests the existence of an orographic effect and/or localized dynamics affecting the local wind.

Now we are in conditions to evaluate to what extent local winds around Tumaco are affecting Tumaco sea level at intraseasonal scale. First, both mean daily zonal local wind and wind-forcing associated to Kelvin waves (Figure S3) are spatially averaged over a region centred at Tumaco (black rectangle in Figure 9a). Then we apply a wavelet transform over both wind time series, and the energy density variance corresponding to the intraseasonal variability (30–90 days) is isolated in both time series (Figure 9b). Note that differently than in Figure 7, in this case we use mean daily sea level data to perform the comparison with daily wind data. Next, the Pearson correlation between both wind intraseasonal signals and the intraseasonal signal of mean daily sea level measured at Tumaco are calculated. Results show that intraseasonal signals of local wind and sea level around Tumaco are weakly correlated (0.07), while the correlation between sea level and the projected wind-forcing associated to Kelvin waves is substantially larger (0.33). Consequently, the intraseasonality we find at Tumaco sea level observations is mostly generated nonlocally, which highlights the ability of the Tumaco tide gauge to capture intraseasonal Kelvin waves propagating from the western Pacific. A similar result is achieved whether daily instantaneous values of sea level are used (e.g., daily sea

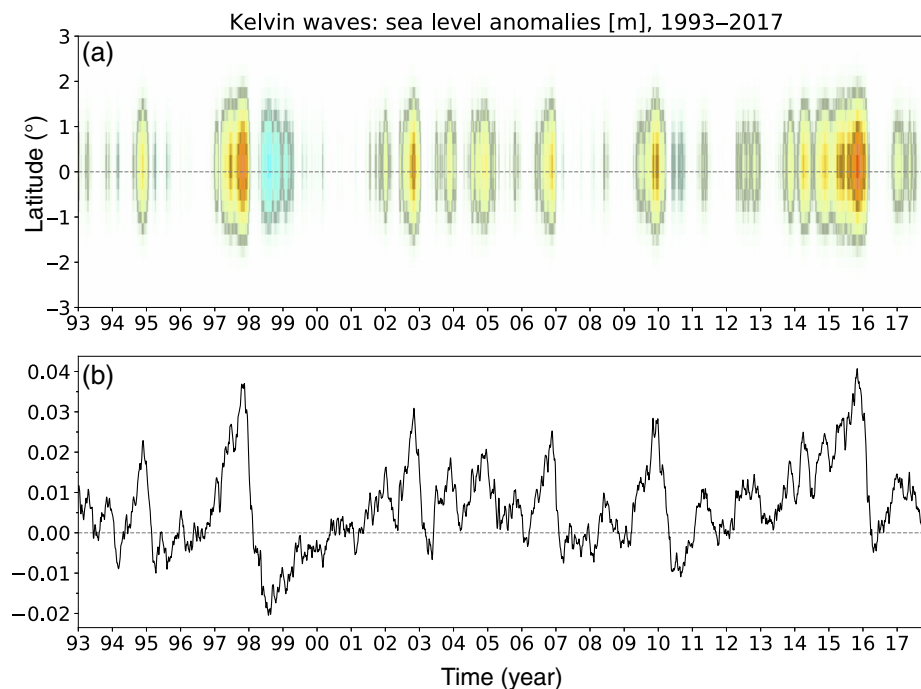


FIGURE 8 (a) Mean meridional structure of Kelvin waves for years 1993–2017. Downwelling and upwelling Kelvin waves correspond to reddish and bluish shading, respectively. (b) Time series of the zonal-averaged Kelvin sea level anomalies over the equatorial Pacific Ocean (between 145°E and the Pacific coast of Colombia). Note that the largest positive peaks in the bottom panel refer to El Niño 1997/1998 and El Niño 2015/2016 [Colour figure can be viewed at wileyonlinelibrary.com]

level at 1200 LST) instead of daily mean sea level (not shown).

To conclude this section, based on the larger explained variance of PC_1 , the better characterization of interannual variability and of individual ENSO events, the good correlation and the convenient time lags against ENSO oceanic indices, as well as the newly added information on intraseasonal Kelvin waves, the TMI4 obtained for the base period 1986–2015 is selected for further analysis (solid grey line in Figure 5d). In the next section we explore its connection with ENSO-induced rainfall anomalies over Colombia.

5 | EVALUATION OF THE POTENTIAL USE OF THE TMI4 TO FORECAST ENSO-INDUCED RAINFALL OVER COLOMBIA

In this section we investigate the relationship between the TMI4 and rainfall over mainland Colombia during ENSO events. First, two rainfall dataset are compared (section 3.6): one based on satellite measurements (PERSIANN-CDR), and another one that additionally includes information from in-situ rain gauges (CHIRPS). Next, the spatial distribution of the highest correlations between TMI4 and rainfall gridded data are analysed over Colombia. Finally, ENSO-induced anomalies are explored and quantified in detail for selected positive and negative extreme ENSO events, distinguishing for all administrative departments of mainland Colombia.

5.1 | Comparison between PERSIANN-CDR and CHIRPS products

The mean accumulated annual rainfall over mainland Colombia for PERSIANN-CDR and CHIRPS dataset is shown in Figure 10 (panels a and b, respectively). As seen, the spatial distribution and the amount of rainfall are in good agreement in both dataset. Rainfall depicts a large spatial variability that oscillates between the ≈ 900 mm collected in La Guajira (red shading in Figure 10 and Table S1), in the northeast of Colombia next to the Caribbean Sea, and the more than 3,000 mm that fall every year in the Colombian Pacific regions, especially in the departments of El Chocó, Valle del Cauca, Cauca and Nariño (purple and dark blue colours in Figure 10 and Table S1). The finest spatial resolution of CHIRPS allows for a more detailed characterization of rainfall over the Andean mountains and the Amazon basin, where PERSIANN-CDR provides less and more rainfall than CHIRPS, respectively.

5.2 | Study of correlation between TMI4 and rainfall products

Next, the potential connection between TMI4 and rainfall over mainland Colombia is assessed through a cross-correlation analysis. The maximum value of the correlation (in absolute value) and its associated lag time between the time series of TMI4 and those of monthly accumulated rain from PERSIANN-CDR and CHIRPS

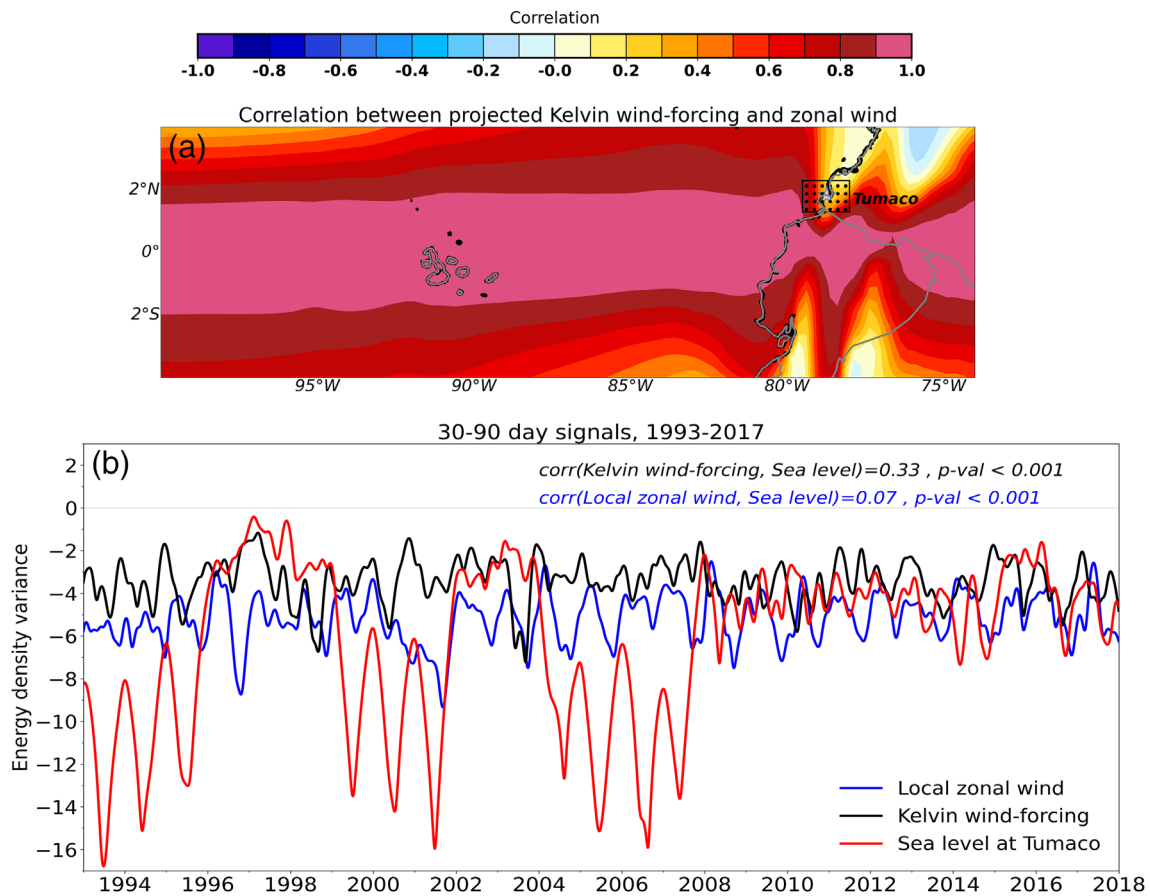
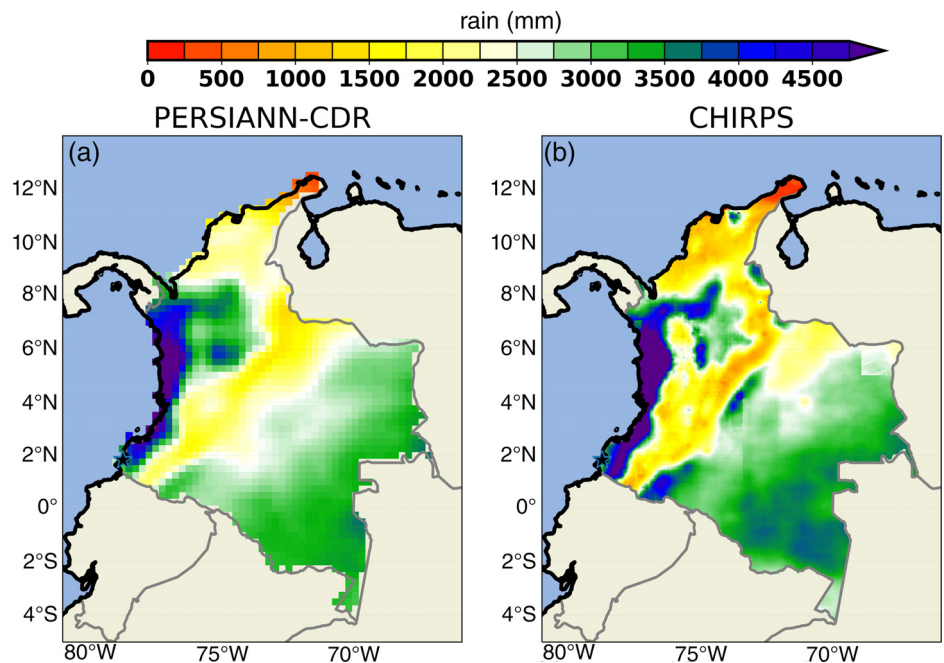


FIGURE 9 (a) Pearson correlation between zonal wind and wind-forcing anomalies associated to the Kelvin mode derived from the Boulanger and Menkes (1995) methodology. The black rectangle illustrates the area around Tumaco used to compute the mean energy density variances displayed in panel (b). (b) Energy density variance at intraseasonal scales from: local zonal wind (solid blue line), wind-forcing associated to the Kelvin mode (solid black line) and sea level measured at Tumaco (solid red line). Pearson correlations at zero lag between sea level at Tumaco and (i) Kelvin wind-forcing and (ii) local zonal wind are shown in the top-right side [Colour figure can be viewed at wileyonlinelibrary.com]

FIGURE 10 Mean accumulated annual rainfall between years 1983 to 2017 (both included) for: (a) PERSIANN-CDR and (b) CHIRPS dataset. Unit in mm [Colour figure can be viewed at wileyonlinelibrary.com]



are plotted for every grid point in Figures 11 and 12, respectively (top panels for the magnitude of largest correlation and bottom panels for the associated lag time). The cross-correlation is performed for a range of time lags of ± 30 months and for two cases: the original rainfall time series, and the rainfall time series without the seasonal component. To remove the seasonality the corresponding climatological accumulated monthly rain for the period 1983–2017 is subtracted to each value of accumulated monthly rain. Note that the mean climatology can be different for every grid cell of each rainfall product. Results shown in Figures 11 and 12 give two interesting insights: first, that correlations are mostly negative (with values between -0.4 and -0.2) except in small regions located in the central and eastern parts of the country and in the southern Pacific coast (Figures 11a,b and 12a,b); second, TMI4 leads the variation of rainfall between 0 and 4 months in northern and central western areas of the country (Figures 11c,d and 12c,d) where correlations are significant (black dots in top panels indicate statistical significance at 99% of confidence level). Note that these areas are the most affected by oceanic conditions. As expected, in Tumaco the relationship between TMI4 and rainfall is simultaneous but positive. Negative correlations indicate that rainfall decreases (increases) when positive (negative) ENSO events develop. Again, the two dataset are in good accordance in both magnitude and time lags distribution. Interestingly, the magnitude of the correlations rises between 0.05 and 0.1 in most regions after seasonal variations are subtracted (Figures 11b and 12b), while in some areas of the northern part of the country time lags are reduced for about 1 month (Figures 11d and 12d), which means that rainfall responds earlier to changes in TMI4. The former result indicates that seasonal variations can play an active role in the delay of ENSO-induced rainfall. The above outcomes illustrate that both dataset perform similarly, but based on the finest characterization of spatial rainfall features, CHIRPS data is hereinafter used for further analysis.

To conclude this section, one unanswered question that we want to respond is whether TMI4 performs better than TMI and ENSO oceanic indices in terms of anticipating rainfall over mainland Colombia. To this end, we have counted the number of CHIRPS grid cells with time lag between $[-6,0)$ months (i.e., those cells which time lag would allow to anticipate rainfall) for two case studies: when seasonality is included, and when it is excluded (correlation and time lag maps between TMI, ENSO 1+2, ENSO 3, ENSO 3.4, ENSO 4, and CHIRPS data are shown in Figures S4–S8). Tables S2 and S3, which also includes a comparison with derived ENSO indices of Takahashi *et al.* (2011) and Sullivan *et al.* (2016), evidences that the

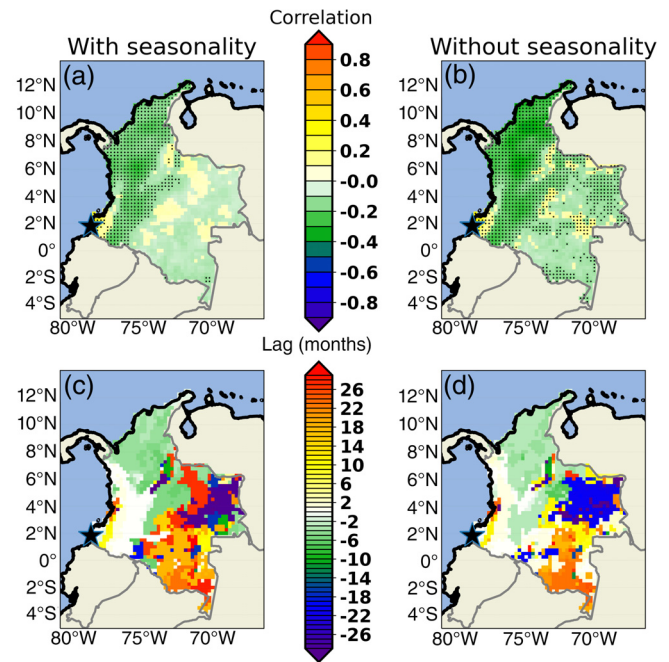


FIGURE 11 (a, b) Maps of cross-correlation between TMI4 and the time series of PERSIANN-CDR rain associated to every grid cell between years 1983 and 2017. The largest correlation (in absolute value) is shown with shading for two cases: (a) with seasonal cycle and (c) without the seasonal cycle. The seasonal cycle has been removed by subtracting the corresponding monthly climatology (1983–2017) to each time series. Black dots indicate that correlations are significant at 99% according to a *t*-Student 2-tailed distribution. Maps of time lag for the above correlation maps are shown in bottom panels for rain data including (c) and not including (d) the seasonal cycle. Negative (positive) time lags mean that TMI4 varies some time earlier (later) than rain (the number of months is indicated in the colorbar). The white colour indicates that variations are nearly simultaneous [Colour figure can be viewed at wileyonlinelibrary.com]

number of grid cells within the selected lag interval is between 23 to $>400\%$ larger, depending on the case, for TMI4 than for the original TMI and ENSO indices (which is equivalent to a surface area between 92,000 and 340,000 km^2), thus confirming that TMI4 is better skilled to anticipate rainfall over Colombia.

5.3 | Characterization of ENSO-induced rainfall anomalies over Colombia

In the following lines, ENSO-induced rainfall anomalies over Colombia are evaluated. ENSO episodes are catalogued into El Niño Canonical, El Niño Modoki, La Niña Canonical and La Niña Modoki following the trimester classification of Navarro-Monterroza *et al.* (2019), which was based on El Niño Modoki index (EMI), as well

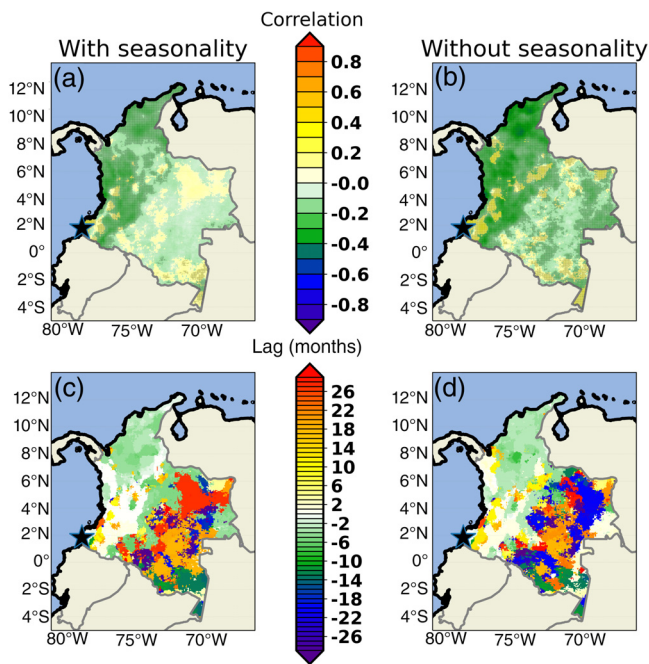


FIGURE 12 (a, b) Maps of cross-correlation between TMI4 and the time series of CHIRPS rain associated to every grid cell between years 1983 and 2017. The largest correlation (in absolute value) is shown with shading for two cases: (a) with seasonal cycle and (c) without the seasonal cycle. The seasonal cycle has been removed by subtracting the corresponding monthly climatology (1983–2017) to each time series. Hash lines indicate that correlations are significant at 99% according to a *t*-Student 2-tailed distribution. Maps of time lag for the above correlation maps are shown in bottom panels for rain data including (c) and not including (d) the seasonal cycle. Negative (positive) time lags mean that TMI4 varies some time earlier (later) than rain (the number of months is indicated in the colorbar). The white colour indicates that variations are nearly simultaneous [Colour figure can be viewed at wileyonlinelibrary.com]

as the Oceanic Niño index (ONI) and ENSO 3, 3.4 and ENSO 4 indices. Those well-defined episodes are depicted over the TMI4 in Figure 13 (see the legend). Note that there are other mixed episodes that were not classified. Departing from the catalogued events mean composites of linearly detrended and deseasoned fields of SST (shading over ocean), surface wind (black arrows) and rain (shading over Colombia) are shown in Figure 14. All fields have been normalized by the associated TMI4 mean index, which gives a good insight of how anomalies growth on average per unit of change of TMI4, as well as the distinguishable mean spatial anomaly patterns associated with general ENSO types. Unsurprisingly, El Niño Canonical is characterized by more intense wind anomalies coming from east/northeast, larger positive SST anomalies, and less rain than El Niño Modoki over large parts of Colombia (Figure 14a). The larger amount of

rainfall around Tumaco associated to El Niño Canonical than to El Niño Modoki is likely explained by the larger amount of moisture carried by wind coming from the Caribbean Sea (see the stronger wind off Tumaco in Figure 14a,b). On the other hand, rainfall anomalies are more sensitive to changes of TMI4 during La Niña events since small variations in the index are reflected in larger rainfall anomalies, being both characterized by strong western wind anomalies at surface levels, although La Niña Modoki is associated with stronger wind anomalies and larger SST negative anomalies off the Pacific Colombian coast (Figure 14c,d). These results are in good accordance with composites of rainfall over Colombia shown by Navarro-Monterroza *et al.* (2019) using rain gauge data. A more detailed picture of mean composited rainfall anomalies and its standard deviation is shown in Figure S10.

The four most extreme positive and negative ENSO events are now analysed in detail (depicted by grey dashed lines in Figure 13): two El Niño (El Niño Canonical 1998 and El Niño Modoki 2015), and two La Niña (La Niña mixed 1996 and La Niña Modoki 2010) episodes. Note that the year that accompanies each event indicates when the peak of TMI4 (in absolute value) was reached. Linearly detrended and deseasoned fields of SST (shading over ocean), surface wind (black arrows) and rain (shading over Colombia) are shown in Figure 15 (see mean fields in Figure S9). The latter provides basic knowledge on surface oceanic and atmospheric anomalous conditions at three different times for selected ENSO events: 6 months before the peak of TMI4 (panels a–d), at the peak of TMI4 (panels e–h) and 6 months after the peak of TMI4 (panels i–l, the associated monthly value of TMI4 is also shown in the title of each panel). As expected, in terms of SST the strongest anomalies (negative for La Niña and positive for El Niño events) are reached at the time of the peak of TMI4, being more notable for 1998 and 2010 events. In contrast, surface wind anomalies show a more variable pattern depending on the considered study case. Unsurprisingly, in the open eastern Pacific basin El Niño events are accompanied by an excess of surface air convergence at the equatorial region (Figure 15b,d,f,h) favoured by the warmer SST (with an increment of 1–3°C). Additionally in the Colombian Pacific coast during both El Niño events and 6 months after the peak of La Niña 1996 appear strong southwestward anomalies (see strong black arrows near Colombia in Figure 15b,d,f,h,i,j), which suggests that the Chocó low-level jet (ChocoJet) is intensely weakened (Serna *et al.*, 2018). This weakening is accompanied by a deficit of rain over mainland Colombia (see brown shading almost covering the whole country in Figure 15i). Conversely, these wind anomalies tend to be very small

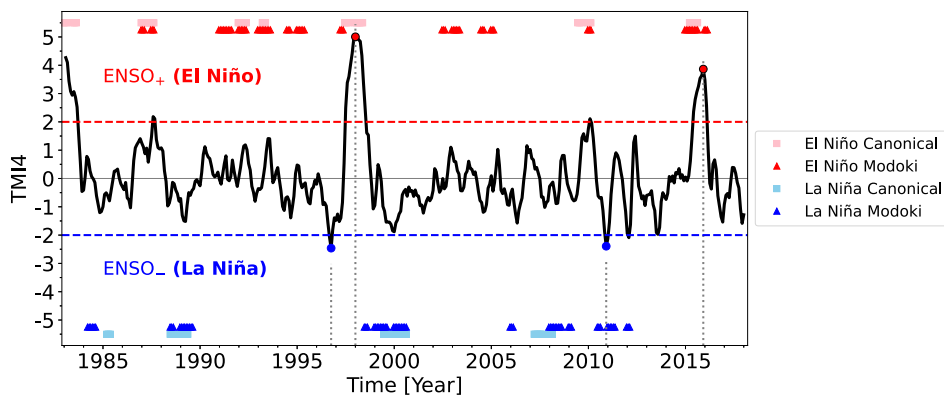


FIGURE 13 Time series of TMI4 for the period 1983–2017. Months classified by ENSO types are depicted with squares and triangles according to the legend. This classification is taken from Navarro-Monterroza *et al.* (2019) (see Table 2 therein). The two strongest positive (El Niño) and negative (La Niña) ENSO events are selected as study cases (indicated by vertical grey dashed lines and circles). Horizontal dashed red and blue lines denote the threshold values of $TMI4 = 2$ and $TMI4 = -2$ respectively, above and below which that most intense Niño and Niña events are distinguished [Colour figure can be viewed at wileyonlinelibrary.com]

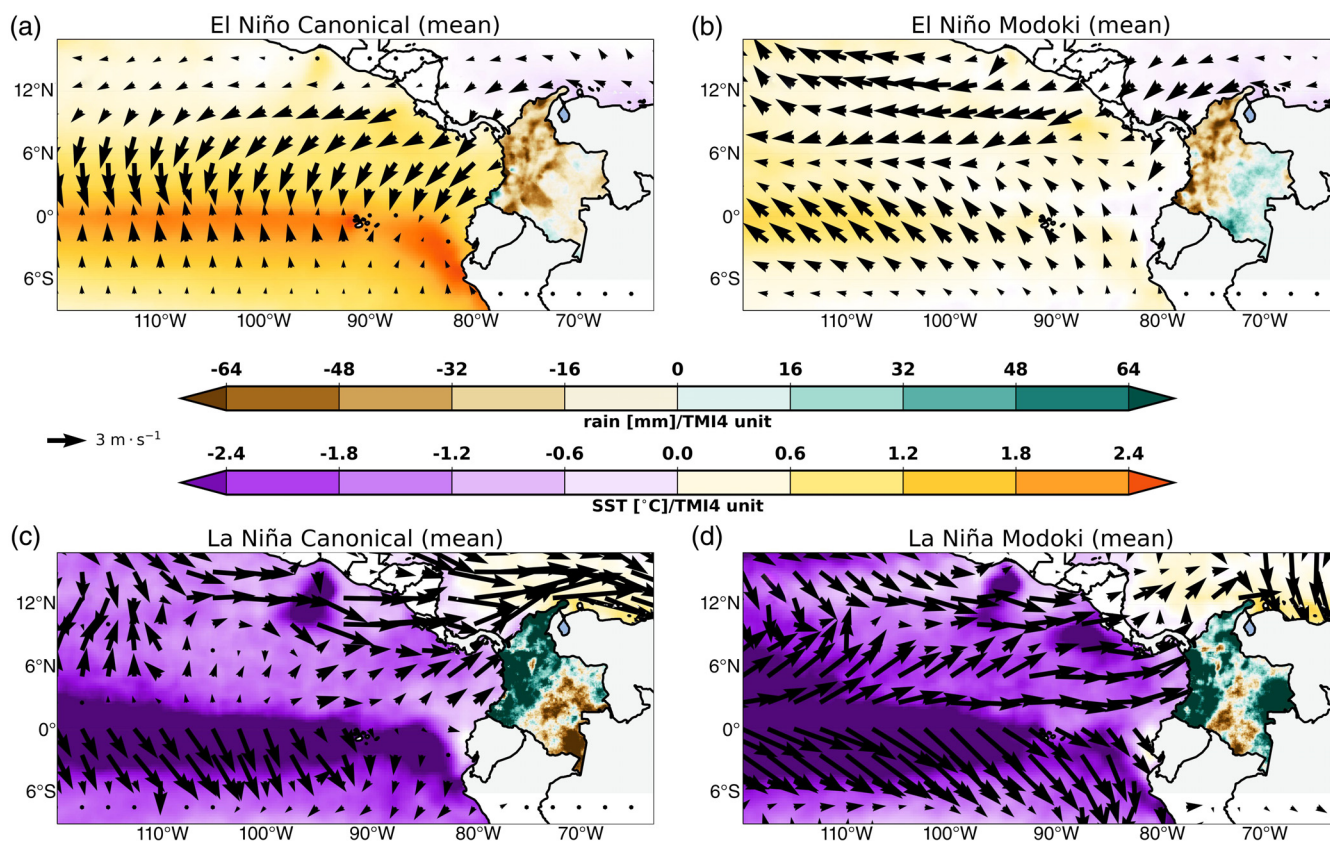


FIGURE 14 Mean composites of surface wind (black arrows), sea surface temperature (SST, purple-red colorbar) and rainfall anomalies (brown-turquoise colorbar) over Colombia according to classified ENSO events depicted in Figure 13. Composites are constructed for the common wind, SST and rainfall period (1993–2017). In this case anomalies are normalized by the associated TMI4 to each trimester included in the construction of the composite, which yield anomalies per unit of TMI4. Note that anomalies are computed by subtracting the linear trend and the monthly climatology at each grid cell. Mean fields of SST and surface wind are shown in Figure S9 [Colour figure can be viewed at wileyonlinelibrary.com]

or even change their sign during La Niña events (Figure 15a,c,e,g,k), thus helping to intensify the ChocoJet.

Regarding the Colombian Caribbean Sea, SST anomalies are smaller (less than 1°C in absolute magnitude). They turn from negative (positive) sign 6 months before

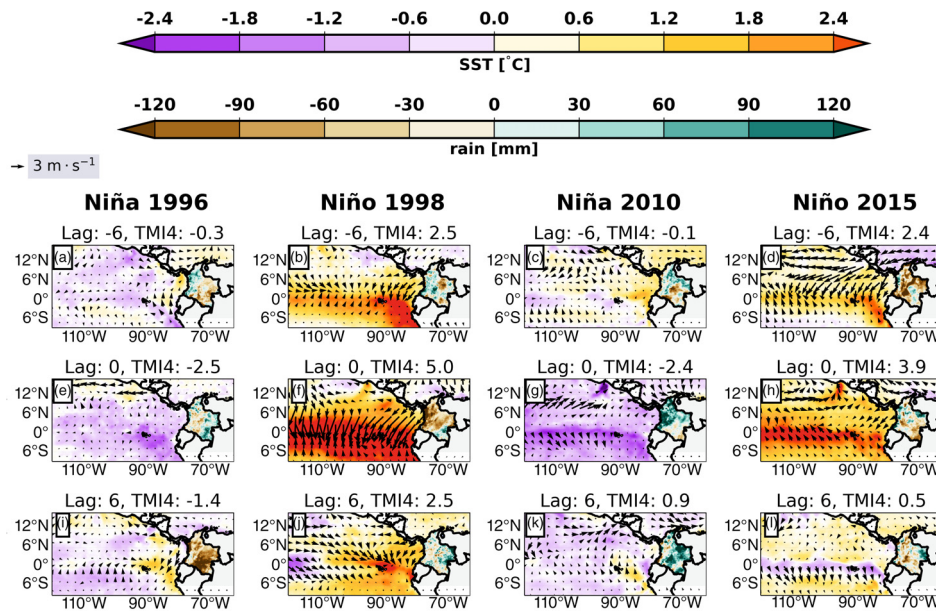
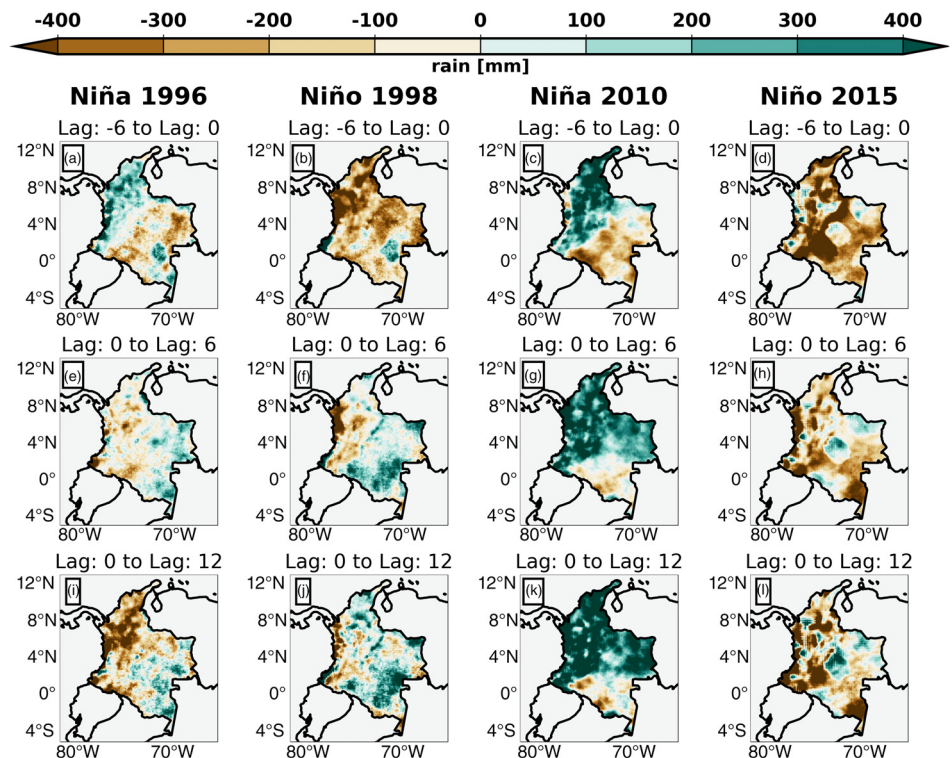


FIGURE 15 Maps showing SST anomalies (purple-red colorbar), surface wind anomalies (black arrows) and rain anomalies over Colombia (brown-turquoise colorbar) for selected ENSO events shown in Figure 13. Anomalies for all variables at every grid cell are defined as the original values without the corresponding monthly climatology and the trend. For each ENSO maps are shown for three different moments: (a–d) 6 months before the TMI4 peak (lag: –6), (e–h) at the TMI4 peak (lag: 0), and (i–l) 6 months after the TMI4 peak (lag: 6). Arrow scale is shown in the top-left. Mean fields of SST and surface wind are shown in Figure S9 [Colour figure can be viewed at wileyonlinelibrary.com]

FIGURE 16 Maps of accumulated rainfall anomalies in Colombia for selected ENSO events shown in Figure 13. Rain anomalies are added up for each event and for three different time intervals: (a–d) from 6 months before the TMI4 peak up to the month of the TMI4 peak (lag: –6 to lag: 0), (e–h) from the month of the TMI4 peak up to 6 months after the peak (lag: 0 to lag: 6), and (i–l) from the month of the TMI4 peak up to 12 months later (lag: 0 to lag: 12). Accumulated rainfall anomalies detailed for each administrative department within mainland Colombia are shown in Table 3. Mean fields of SST and surface wind are shown in Figure S9. Mean rainfall is shown in Table S1 for every administrative department [Colour figure can be viewed at wileyonlinelibrary.com]



the peak to positive (negative) 6 months after the peak of El Niño (La Niña) events here considered. Surface wind anomalies show a more complex behaviour that differs

for each event: small eastward anomalies 6 months before the peak of La Niña episodes (Figure 15a,c) and weak northeastward and large southwestward anomalies

TABLE 3 Mean accumulated rainfall anomalies from CHIRPS data for the selected ENSO events displayed in Figure 13 [Colour table can be viewed at wileyonlinelibrary.com]

Department	Niña 1996 [mm]			Niño 1998 [mm]			Niña 2010 [mm]			Niño 2015 [mm]		
	[-6, 0]	[0, 6]	[0, 12]	[-6, 0]	[0, 6]	[0, 12]	[-6, 0]	[0, 6]	[0, 12]	[-6, 0]	[0, 6]	[0, 12]
Amazonas	31	121	95	-130	78	11	-141	-56	-9	-187	-233	-259
Antioquia	221	-108	-440	-416	-178	14	394	457	498	-272	-278	-325
Arauca	154	43	-82	-279	130	122	125	370	407	-270	95	20
Atlántico	49	-39	-257	-237	18	101	607	238	709	-453	-65	-2
Bolívar	219	-71	-371	-395	2	161	616	445	697	410	-198	-316
Boyacá	17	-44	-172	-219	50	120	280	362	479	-250	-53	-52
Córdoba	253	-65	-222	-233	-75	-19	264	329	372	-132	10	32
Caldas	101	-204	-518	-404	-231	-50	442	536	728	-412	358	-469
Caquetá	-140	-98	-115	-138	200	179	-172	6	-37	-584	-160	-250
Casanare	-119	-5	-152	-320	82	17	112	327	380	-453	-2	58
Cauca	199	-42	-80	-88	-70	47	195	391	532	-330	-323	-696
Cesar	216	-63	-351	-372	40	174	668	427	760	-300	165	-116
Chocó	278	-67	-535	-763	-509	-370	95	675	852	-77	-547	-410
Cundinamarca	-1	-97	-226	-205	-58	-19	214	391	523	-319	-68	-70
Guainía	-138	114	38	-237	-4	43	-112	264	401	-293	-192	-45
Guaviare	-37	-37	69	-48	157	226	-209	54	133	-350	-161	-47
Huila	-2	-41	-149	-225	-167	-146	285	461	674	-442	-262	-335
La Guajira	-31	23	-136	-219	51	66	519	362	650	-397	-52	-39
Magdalena	150	3	-231	-296	41	187	576	360	723	-548	-176	-244
Meta	-79	23	46	-210	42	50	-40	284	316	-364	11	16
Nariño	51	-294	-283	436	201	273	185	373	544	-149	-251	-642
Norte de Santander	126	176	-28	-344	-18	100	599	612	742	-576	-167	-339
Putumayo	-242	-176	-384	-312	130	81	-315	32	67	-607	-376	-300
Quindío	136	-30	-144	-211	-157	-66	397	365	558	-336	-56	-13
Risaralda	45	-177	-395	-358	-210	-132	501	491	765	-169	-121	-121
Santander	142	-92	-230	-257	-58	46	491	406	583	-270	-116	-268
Sucre	255	11	-255	-376	52	197	599	429	702	-398	-131	-311
Tolima	65	-79	-273	-285	-118	-16	372	463	650	-452	-237	-268
Valle del Cauca	270	7	-185	-339	-120	-91	222	393	537	-563	-201	-399
Vaupés	69	80	140	79	283	311	-239	-28	-34	-189	-302	-206
Vichada	-119	110	-6	-188	119	135	6	313	448	-139	-18	2

Note: The information is provided for mainland Colombia administrative departments (identified by the same colours that appear in Figure 1b, note that we have excluded the department of San Andrés and Providencia Caribbean islands, as well as Malpelo and Gorgona Pacific islands). The corresponding monthly climatology rainfall has been subtracted to compute the anomalies as in Figures 14 and 15. Anomalies around the TMI4 maximum (or minimum for Niña events) have been added up for three cases: the previous 6 months before the peak ([-6, 0], including the month of the peak), the following 6 months after the peak ([0, 6], including the month of the peak), and the following 12 months after the peak ([0, 12], including the month of the peak). Blue and red numbers indicate positive and negative rain anomalies with respect the monthly climatology, respectively. Unit in mm.

for El Niño 1998 and 2015, respectively (Figure 15b,d). At the peak of TMI4, anomalies are very weak for La Niña 1996 and El Niño 1998 (Figure 15e,f, respectively), and strongly southeastward and northwestward for La Niña 2010 and El Niño 2015, respectively (Figure 15g,h). La Niña 2010 is an example of amplified convergence

between the easterlies and the ChocoJet (Figure 15g), thus favouring large amounts of exceeding rain in the northern and western areas of Colombia (see turquoise shading in Figure 15g).

A more detailed view of rainfall anomalies over mainland Colombia is provided in Figure 16, in which

anomalies have been integrated at each grid cell of CHIRPS data considering three time intervals: from 6 months before until the month of TMI4 peak (both months included, panels a–d), from the month of TMI4 peak until 6 months later (both months included, panels e–l), and from the month of TMI4 peak until 12 months later (both months included, panels e–l). Results indicate that months before the peak of TMI4 is reached rainfall responds as expected, with overall positive (negative) anomalies in the north and western areas of Colombia for La Niña (El Niño) events (Figure 16a–d). However, the persistence of these anomalies after the peak of the TMI4 depends on the associated atmospheric and oceanic conditions of each individual event, thus anomalies become negative for La Niña 1996 and strongly positive for La Niña 2010 (Figure 16e,g,i,k). Note that the extreme La Niña 2010 was followed by another extreme La Niña event in 2011, thus strengthening the conditions for the large excess of rain captured months later (Hoyos *et al.*, 2013). Also integrated rainfall anomalies show a large variety of values during El Niño events, in which some northern and western areas show positive rainfall anomalies after the TMI4 peak (Figure 16f,h,j,i).

Table 3 shows the integrated rainfall anomalies averaged by administrative departments (identified by the same colours as in Figure 1b) for selected ENSO events (see climatological mean rainfall in Table S1). Chocó and César departments led the excess of rain within 6 months before the TMI4 peak of La Niña 1996 and La Niña 2010, respectively (with 278 and 668 mm each of them). In contrast, Putumayo showed the largest negative anomalies in both cases (–242 and –315 mm respectively). Notably, during El Niño 1998 Chocó had the largest negative anomalies for all periods, with accumulated anomalies of –763 mm and –509 mm 6 months before and 6 months after the peak of TMI4, thus supporting the intense weakening of ChocoJet during this event observed in Figure 16b,f,j. The department of Nariño (located in the southwestern part of Colombia, next to Ecuador, Figure 1b) had large amounts of rainfall during the development of El Niño 1998 (accumulated excess of 436 mm before the peak of TMI4) likely favoured by local deep convection induced by the extremely warm SST found there (Figure 16f). Other departments located in the southeastern side of Colombia such as Amazonas and Vaupés behave differently and the range of anomalies induced by ENSO events are more moderate (within ± 300 mm) since are located east of the Andean Mountains and also are strongly influenced by the South American monsoon and associated low-level jets.

To conclude this section, results shown illustrate the potential of a well-located pointwise index such as TMI4 to be used as an indicator of the sign of rainfall anomalies during the development of ENSO events (i.e., before the

peak of TMI4 is reached). After the peak, rainfall anomalies show a variability that strongly depends on regional patterns such as SST and wind anomalies in both Pacific and Caribbean basins. Some suggestions to improve the performance of TMI4 are proposed in the next section.

6 | CONCLUSIONS

This work has described a point-wise climate index located at Tumaco, in the southwestern Colombian Pacific basin, which we have named as TMI4. The original TMI index (Rodríguez-Rubio, 2013) was already constructed about one decade ago departing from time series of SST, AT and monthly rain. Despite this index was able to capture the strong interannual variability associated with ENSO events, it had a delay of 1–2 months with respect to ENSO regional indices based on SST, which limited its potential applicability. The availability of sea level observations at Tumaco has allowed the TMI4 construction (Figure 5d). As we have shown in Table 1, the time delay with El Niño indices has been reduced to about a month with respect to the TMI, and the residual component of the TMI4 (TMI4_r) even captures earlier the ENSO induced variability than the ENSO 3 index (Table 2). The reason of this improvement is the new dynamical information added by sea level data at intraseasonal scale (30–90 days), which incorporates local sea level variations induced by downwelling Pacific equatorial Kelvin waves generated during the onset of El Niño. These waves travel from the western Pacific Ocean towards the central and eastern Pacific (Figure 8) and are detected at Tumaco, being minimally disturbed by local wind at intraseasonal scale (Figure 9). However, the imprint of waves is a bit noisy and likely less energetic than in open ocean due to the proximity of the Tumaco tide gauge to the coast (Figure 7). To avoid this problem and to better capture Kelvin waves, one interesting option is to install complementary tide gauge or buoy in Gorgona Island, which is located very close to the equatorial band ($\sim 3^\circ\text{N}$), 28 km off the Pacific coast of Colombia. This may allow to detect a less noisy signal of equatorial Kelvin waves that can be contrasted against measurements made at Tumaco tide gauge.

Next, we have evaluated the potential usefulness of TMI4 to predict ENSO-induced rainfall over mainland Colombia. To this end, two rainfall products have been first compared (PERSIANN-CDR and CHIRPS), and then cross-correlated against TMI4 (Figures 11 and 12). Significant negative cross-correlations have been found in extensive western and northern areas of Colombia, with lag times of about 0–6 months in which TMI4 leads the variability. From a detailed analysis of four extreme ENSO events (Figure 13), we have found that TMI4 is

potentially useful to predict the sign of rainfall anomalies those months before the peak of the event has been reached, especially in northern and western departments of Colombia where large positive and negative rainfall anomalies are observed during the development of La Niña and El Niño events, respectively (Figure 15 and Table 3). After that time, rainfall shows large variations that, to a large extent, depend on the magnitude of SST anomalies in the Pacific coast of Colombia, the interbasin western Pacific–Caribbean SST and AT gradients, the season, the strength and position of the Chocó low-level jet (ChocoJet) or the trade winds in the Caribbean Sea. Therefore, to better predict the sign of the rainfall over Colombia, and to refine the magnitude of the expected rainfall we find necessary the use of complementary information on the state of SST gradients and surface wind fields in Pacific and Caribbean Colombian basins, as suggested by Cerón *et al.* (2021a). In this regard, a next study aimed to assess the performance of TMI4 under operational conditions for the diversity of ENSO events is planned (note that a brief introduction to its operational implementation is available in Appendix).

Finally, we would like to mention that a modified TMI4 version including the eastern Pacific 20°C isotherm depth provided by the Tropical Atmosphere Ocean project has been explored (Figures S11–S14 and Tables S4–S6), but it has been discarded due to its lower ability to anticipate rainfall anomalies over Colombia in comparison to the TMI4 here analysed. The main reason is that time series of 20°C isotherm depth are notably shorter (from 1981 instead of 1961 for Tumaco-based data), which adds too much weight to El Niño 1998, in addition to the existence of some gaps. However, in the mid-term we expect that, when the length of time series gets longer, the information provided by this data on eastern Pacific thermocline depth variation will be useful to enhance TMI4 performance.

AUTHOR CONTRIBUTIONS

Juan-Manuel Sayol: Conceptualization; data curation; formal analysis; investigation; methodology; software; visualization; writing – original draft; writing – review and editing. **Laura M. Vásquez:** Data curation; methodology; supervision; writing – review and editing. **Jorge L. Valencia:** Software; visualization; writing – review and editing. **Jean R. Linero-Cueto:** Writing – review and editing. **David García-García:** Writing – review and editing. **Isabel Vigo:** Writing – review and editing. **Alejandro Orfila:** Writing – review and editing.

ACKNOWLEDGEMENTS

J. M. Sayol, L. M. Vásquez and J. L. Valencia thank funding from Centro de Investigaciones Oceanográficas e

Hidrográficas del Pacífico – Dirección General Marítima de Colombia (Dimar), Ministry of National Defense of Colombia. J. M. Sayol also thanks the joint funding received from the Generalitat Valenciana and the European Social Fund under Grant APOSTD/2020/254. The work of DGG and IV was partially supported by Spanish Project RTI2018-093874-B-100 funded by MCIN/AEI/10.13039/501100011033 and by the Generalitat Valenciana Grant PROMETEO/2021/030. A. Orfila acknowledges financial support from FEDER/Ministerio de Ciencia, Innovación y Universidades – Agencia Estatal de Investigación through MOCCA project (grant # RTI2018-093941-B-C31). We appreciate the collaboration of the University of Magdalena, through the CITEPT research group (Science and Technology for Tropical Fisheries, for its acronym in Spanish).

CONFLICT OF INTEREST

The authors declare no potential conflict of interest.

ORCID

Juan-Manuel Sayol  <https://orcid.org/0000-0003-3319-2910>

REFERENCES

- Akaike, H. (1974) A new look at the statistical model identification. *IEEE Transactions on Automatic Control*, 19, 716–723.
- Amador, J. (2008) The intra-americas sea low-level jet. *Annals of the New York Academy of Sciences*, 1146, 153–188.
- Amador, J.A. (1998) A climate feature of the tropical americas: the trade wind easterly jet. *Temas Meteorológicos y Oceanográficos*, 5, 91–102.
- Andrade, C.A. (1993) Análisis de la velocidad del viento en el mar caribe. *Boletín Científico CIOH*, 13, 33–43.
- Andrade, C.A. and Barton, E.D. (2009) The atmospheric low level jet and the surface mesoscale circulation of the Caribbean Sea. *GEOS*, 29, 85.
- Arias, P.A., Martínez, J.A. and Vieira, S.C. (2015) Moisture sources to the 2010–2012 anomalous wet season in northern South America. *Climate Dynamics*, 45, 2861–2884. <https://doi.org/10.1007/s00382-015-2511-7>.
- Banzon, V., Smith, T.M., Chin, T.M., Liu, C. and Hankins, W. (2016) A long-term record of blended satellite and in situ sea-surface temperature for climate monitoring, modeling and environmental studies. *Earth System Science Data*, 8, 165–176.
- Barón-Leguizamón, A. (2003) Modelos geoespaciales de la distribución de las variables climatológicas en el territorio colombiano. *Meteorología Colombiana*, 7, 81–89.
- Boulangier, J.-P. and Menkes, C. (1995) Propagation and reflection of long equatorial waves in the Pacific Ocean during the 1992–1993 El Niño. *Journal of Geophysical Research: Oceans*, 100, 25041–25059.
- Brockwell, P.J. and Davis, R.A. (1993) *Time Series: Theory and Methods*. New York, NY: Springer.
- Cai, W., McPhaden, M.J., Grimm, A.M., Rodrigues, R.R., Taschetto, A.S., Garreaud, R.D., Dewitte, B., Poveda, G.,

- Ham, Y.-G., Santoso, A., Ng, B., Anderson, W., Wang, G., Geng, T., Jo, H.-S., Marengo, J.A., Alves, L.M., Osman, M., Li, S., Wu, L., Karamperidou, C., Takahashi, K. and Vera, C. (2020) Climate impacts of the El Niño–Southern Oscillation on South America. *Nature Reviews Earth & Environment*, 1, 215–231. <https://doi.org/10.1038/s43017-020-0040-3>.
- Caldwell, P. C. and Merrifield, M. A. (2015) Joint archive for sea level (JASL). Data report: October 2015. Joint Institute for Marine and Atmospheric Research. JIMAR contribution no. 15-392. Data report no. 24. Available at: <http://ilikai.soest.hawaii.edu/UHSLC/jasl/datrep/JASL2015DataReport.pdf>. The JASL is archived at the National Oceanographic Data Center: <http://data.nodc.noaa.gov/cgi-bin/iso?id=gov.noaa.nodc:0019568>.
- Canchala, T., Alfonso-Morales, W., Carvajal-Escobar, Y., Cerón, W. L. and Caicedo-Bravo, E. (2020a) Monthly rainfall anomalies forecasting for southwestern Colombia using artificial neural networks approaches. *Water*, 12, 2628.
- Canchala, T., Alfonso-Morales, W., Cerón, W.L., Carvajal-Escobar, Y. and Caicedo-Bravo, E. (2020b) Teleconnections between monthly rainfall variability and large-scale climate indices in southwestern Colombia. *Water*, 12, 1863.
- Canchala, T., Loaiza Cerón, W., Francés, F., Carvajal-Escobar, Y., Andreoli, R.V., Kayano, M.T., Alfonso-Morales, W., Caicedo-Bravo, E. and Ferreira de Souza, R.A. (2020c) Streamflow variability in Colombian Pacific basins and their teleconnections with climate indices. *Water*, 12, 526.
- Capotondi, A., Wittenberg, A.T., Newman, M., Lorenzo, E.D., Yu, J.-Y., Braconnot, P., Cole, J., Dewitte, B., Giese, B., Guilyardi, E., Jin, F.-F., Karneuskas, K., Kirtman, B., Lee, T., Schneider, N., Xue, Y. and Yeh, S.-W. (2015) Understanding ENSO diversity. *Bulletin of the American Meteorological Society*, 96, 921–938.
- Cerón, W.L., Andreoli, R.V., Kayano, M. and Avila-Diaz, A. (2021a) Role of the eastern pacific caribbean sea sst gradient in the Choco low-level jet variations from 1900–2015. *Climate Research*, 83, 61–74.
- Ceron, W.L., Carvajal-Escobar, Y., Andreoli, R.V., Kayano, M. and González, N. (2020) Spatio-temporal analysis of the droughts in Cali, Colombia and their primary relationships with the El Niño–Southern Oscillation (ENSO) between 1971 and 2011. *Atmosfera*, 33, 51–69.
- Cerón, W.L., Kayano, M.T., Andreoli, R.V., Canchala, T., Carvajal-Escobar, Y. and Alfonso-Morales, W. (2021b) Rainfall variability in southwestern Colombia: changes in ENSO-related features. *Pure and Applied Geophysics*, 178, 1087–1103.
- Chiew, F.H.S. and McMahon, T.A. (2002) Global ENSO–streamflow teleconnection, streamflow forecasting and interannual variability. *Hydrological Sciences Journal*, 47, 505–522. <https://doi.org/10.1080/02626660209492950>.
- Codiga, D.L. (2011) *Unified tidal analysis and prediction using the UTide Matlab functions*. South Kingstown, RI: University of Rhode Island, Technical report 2011-01.
- Contreras, D., Voets, A., Junghardt, J., Bhamidipati, S. and Contreras, S. (2020) The drivers of child mortality during the 2012–2016 drought in La Guajira, Colombia. *International Journal of Disaster Risk Reduction*, 11, 87–104. <https://doi.org/10.1007/s13753-020-00255-0>.
- Córdoba-Machado, S., Palomino-Lemus, R., Gámiz-Fortis, S.R., Castro-Díez, Y. and Esteban-Parra, M.J. (2015) Influence of tropical Pacific SST on seasonal precipitation in Colombia: prediction using El Niño and El Niño Modoki. *Climate Dynamics*, 44, 1293–1310. <https://doi.org/10.1007/s00382-014-2232-3>.
- D'Arrigo, R., Cook, E.R., Wilson, R.J., Allan, R. and Mann, M.E. (2005) On the variability of enso over the past six centuries. *Geophysical Research Letters*, 32, L03711.
- Delcroix, T., Picaut, J. and Eldin, G. (1991) Equatorial Kelvin and Rossby waves evidenced in the Pacific Ocean through GEOSAT sea level and surface current anomalies. *Journal of Geophysical Research, Oceans*, 96, 3249–3262.
- Diaz, H.F., Hoerling, M.P. and Eischeid, J.K. (2001) ENSO variability, teleconnections and climate change. *International Journal of Climatology*, 21, 1845–1862. <https://doi.org/10.1002/joc.631>.
- Durán-Quesada, A.M., Gimeno, L. and Amador, J. (2017) Role of moisture transport for central american precipitation. *Earth System Dynamics*, 8, 147–161.
- Emery, W.J. and Thomson, R.E. (2001) Time-series analysis methods. In: Emery, W.J. and Thomson, R.E. (Eds.) *Data Analysis Methods in Physical Oceanography*. Amsterdam: Elsevier, pp. 371–567.
- Espinoza, J.C., Garreaud, R., Poveda, G., Arias, P.A., Molina-Carpio, J., Masiokas, M., Viale, M. and Scaff, L. (2020) Hydroclimate of the Andes part I: Main climatic features. *Frontiers in Earth Science*, 8, 64.
- Esquivel, A., Llanos-Herrera, L., Agudelo, D., Prager, S.D., Fernandes, K., Rojas, A., Valencia, J.J. and Ramirez-Villegas, J. (2018) Predictability of seasonal precipitation across major crop growing areas in Colombia. *Climate Services*, 12, 36–47.
- Fang, X.-H. and Mu, M. (2018) Both air–sea components are crucial for El Niño forecast from boreal spring. *Scientific Reports*, 8, 10501. <https://doi.org/10.1038/s41598-018-28964-z>.
- Funk, C., Peterson, P., Landsfeld, M., Pedreros, D., Verdin, J., Shukla, S., Husak, G., Rowland, J., Harrison, L., Hoell, A. and Michaelsen, J. (2015) The climate hazards infrared precipitation with stations—a new environmental record for monitoring extremes. *Scientific Data*, 2, 150066. <https://doi.org/10.1038/sdata.2015.66>.
- Grimm, A.M. and Tedeschi, R.G. (2009) ENSO and extreme rainfall events in South America. *Journal of Climate*, 22, 1589–1609. <https://doi.org/10.1175/2008JCLI2429.1>.
- Hackert, E., Ballabrera-Poy, J., Busalacchi, A.J., Zhang, R.-H. and Murtugudde, R. (2007) Comparison between 1997 and 2002 El Niño events: role of initial state versus forcing. *Journal of Geophysical Research, Oceans*, 112, C01005.
- Handoh, I.C., Matthews, A.J., Bigg, G.R. and Stevens, D.P. (2006) Interannual variability of the tropical Atlantic independent of and associated with ENSO: part I. The north tropical Atlantic. *International Journal of Climatology*, 26, 1937–1956. <https://doi.org/10.1002/joc.1343>.
- Hanley, D.E., Bourassa, M.A., O'Brien, J.J., Smith, S.R. and Spade, E.R. (2003) A quantitative evaluation of ENSO indices. *Journal of Climate*, 16, 1249–1258. [https://doi.org/10.1175/1520-0442\(2003\)16<1249:AQEOEI>2.0.CO;2](https://doi.org/10.1175/1520-0442(2003)16<1249:AQEOEI>2.0.CO;2).
- He, X., Pan, M., Wei, Z., Wood, E.F. and Sheffield, J. (2020) A global drought and flood catalogue from 1950 to 2016. *Bulletin of the American Meteorological Society*, 101, E508–E535. <https://doi.org/10.1175/BAMS-D-18-0269.1>.
- Hirabayashi, Y., Kanae, S., Emori, S., Oki, T. and Kimoto, M. (2008) Global projections of changing risks of floods and droughts in a

- changing climate. *Hydrological Sciences Journal*, 53, 754–772. <https://doi.org/10.1623/hysj.53.4.754>.
- Hoyos, N., Escobar, J., Restrepo, J., Arango, A. and Ortiz, J. (2013) Impact of the 2010–2011 La Niña phenomenon in Colombia, South America: the human toll of an extreme weather event. *Applied Geography*, 39, 16–25.
- Huthnance, J.M. (1978) On coastal trapped waves: analysis and numerical calculation by inverse iteration. *Journal of Physical Oceanography*, 8, 74–92. [https://doi.org/10.1175/1520-0485\(1978\)008<0074:OCTWAA>2.0.CO;2](https://doi.org/10.1175/1520-0485(1978)008<0074:OCTWAA>2.0.CO;2).
- Kousky, V.E. and Higgins, R.W. (2007) An alert classification system for monitoring and assessing the ENSO cycle. *Weather and Forecasting*, 22, 353–371. <https://doi.org/10.1175/WAF987.1>.
- L'Heureux, M.L., Takahashi, K., Watkins, A.B., Barnston, A.G., Becker, E.J., Liberto, T.E.D., Gamble, F., Gottschalck, J., Halpert, M. S., Huang, B., Mosquera-Vásquez, K. and Wittenberg, A.T. (2017) Observing and predicting the 2015/16 El Niño. *Bulletin of the American Meteorological Society*, 98, 1363–1382.
- Liu, Y., San Liang, X. and Weisberg, R.H. (2007) Rectification of the bias in the wavelet power spectrum. *Journal of Atmospheric and Oceanic Technology*, 24, 2093–2102. <https://doi.org/10.1175/2007JTECH0511.1>.
- Marcos, M. and Tsimplis, M.N. (2007) Variations of the seasonal sea level cycle in southern Europe. *Journal of Geophysical Research, Oceans*, 112, C12011.
- Martínez, C., Goddard, L., Kushnir, Y. and Ting, M. (2019) Seasonal climatology and dynamical mechanisms of rainfall in the Caribbean. *Climate Dynamics*, 53, 825–846. <https://doi.org/10.1007/s00382-019-04616-4>.
- Martís, A., van Oldenborgh, G.J. and Burgers, G. (2002) Predicting rainfall in the Dutch Caribbean—more than El Niño? *International Journal of Climatology*, 22, 1219–1234. <https://doi.org/10.1002/joc.779>.
- Moy, C.M., Seltzer, G.O., Rodbell, D.T. and Anderson, D.M. (2002) Variability of El Niño/Southern Oscillation activity at millennial timescales during the holocene epoch. *Nature*, 420, 162–165. <https://doi.org/10.1038/nature01194>.
- Mysak, L.A. (1980) Topographically trapped waves. *Annual Review of Fluid Mechanics*, 12, 45–76. <https://doi.org/10.1146/annurev.fl.12.010180.000401>.
- Navarro-Monterroza, E.A.-A., Arias, P.A. and Vieira, S.C. (2019) El Niño-Oscilación del Sur, fase Modoki, y sus efectos en la variabilidad espacio-temporal de la precipitación en Colombia. *Revista de la Academia Colombiana de Ciencias Exactas, Físicas y Naturales*, 43, 120–132.
- Nguyen, P., Shearer, E.J., Tran, H., Ombadi, M., Hayatbini, N., Palacios, T., Huynh, P., Braithwaite, D., Updegraff, G., Hsu, K., Kuligowski, B., Logan, W.S. and Sorooshian, S. (2019) The chrs data portal, an easily accessible public repository for persiann global satellite precipitation data. *Scientific Data*, 6, 180296. <https://doi.org/10.1038/sdata.2018.296>.
- Okumura, Y. and Xie, S.-P. (2006) Some overlooked features of tropical Atlantic climate leading to a new Niño-like phenomenon. *Journal of Climate*, 19, 5859–5874. <https://doi.org/10.1175/JCLI3928.1>.
- Orfila, A., Álvarez, A., Tintoré, J., Jordi, A. and Basterretxea, G. (2005) Climate teleconnections at monthly time scales in the Ligurian Sea inferred from satellite data. *Progress in Oceanography*, 66, 157–170.
- Orfila, A., Urbano-Latorre, C.P., Sayol, J.M., Gonzalez-Montes, S., Caceres-Euse, A., Hernández-Carrasco, I. and Muñoz, A.G. (2021) On the impact of the Caribbean counter current in the Guajira upwelling system. *Frontiers in Marine Science*, 8, 128. <https://doi.org/10.3389/fmars.2021.626823>.
- Pinilla Herrera, M.C. and Pinzón Correa, C.A. (2016) An assessment of El Niño and La Niña impacts focused on monthly and seasonal rainfall and extreme dry/precipitation events in mountain regions of Colombia and México. *Advances in Geosciences*, 42, 23–33.
- Poveda, G., Álvarez, D.M. and Rueda, O.A. (2010) Hydro-climatic variability over the Andes of Colombia associated with ENSO: a review of climatic processes and their impact on one of the earth's most important biodiversity hotspots. *Climate Dynamics*, 36, 2233–2249.
- Poveda, G. and Mesa, O. (1999) La corriente de chorro superficial del oeste (“del chocó”) y otras dos corrientes de chorro en Colombia: climatología y variabilidad durante las fases del ENSO. *Revista de la Academia Colombiana de Ciencias Exactas, Físicas y Naturales*, 23, 517–528.
- Poveda, G. and Mesa, O.J. (2000) On the existence of Iloró (the rainiest locality on earth): Enhanced ocean–land–atmosphere interaction by a low-level jet. *Geophysical Research Letters*, 27, 1675–1678. <https://doi.org/10.1029/1999GL006091>.
- Poveda, G., Velez, J.I., Mesa, O.J., Mejía, C.D. and Marco, O.J. (2002) Influencia de fenómenos macro climáticos sobre el ciclo anual de la hidrología colombiana: cuantificación lineal, no lineal y percentiles probabilísticos. *Meteorología Colombiana*, 6, 121–130.
- Puertas, O. and Carvajal, Y. (2008) Incidencia de el Niño–oscilación del sur en la precipitación y la temperatura del aire en Colombia utilizando el climate explorer. *Ingeniería y Desarrollo*, 23, 104–118.
- Raikes, J., Smith, T.F., Jacobson, C. and Baldwin, C. (2019) Pre-disaster planning and preparedness for floods and droughts: a systematic review. *International Journal of Disaster Risk Science*, 38, 101207.
- Rodríguez-Rubio, E. (2013) A multivariate climate index for the western coast of Colombia. *Advances in Geosciences*, 33, 21–26.
- Rueda, B.J., Rodríguez, E. and Ortiz, J. (2007) Caracterización espacio temporal del campo de vientos superficiales del Pacífico colombiano y el golfo de Panamá a partir de sensores remotos y datos in situ. *Boletín Científico CCCP*, 14, 49–68.
- Rydbeck, A.V., Jensen, T.G. and Flatau, M. (2019) Characterization of intraseasonal Kelvin waves in the equatorial Pacific Ocean. *Journal of Geophysical Research, Oceans*, 124, 2028–2053. <https://doi.org/10.1029/2018JC014838>.
- Serna, L.M., Arias, P.A. and Vieira, S.C. (2018) Las corrientes superficiales de chorro del chocó y el Caribe durante los eventos de El Niño y El Niño Modoki. *Revista de la Academia Colombiana de Ciencias Exactas, Físicas y Naturales*, 42, 410–421.
- Shimizu, M.H., Ambrizzi, T. and Liebmann, B. (2017) Extreme precipitation events and their relationship with ENSO and MJO phases over northern South America. *International Journal of Climatology*, 37, 2977–2989. <https://doi.org/10.1002/joc.4893>.
- Souza, E.B. and Ambrizzi, T. (2002) ENSO impacts on the South American rainfall during 1980s: Hadley and Walker circulation. *Atmosfera*, 15, 105–120.

- Storch, H.V. and Zwiers, F.W. (1999) *Statistical Analysis in Climate Research*. Cambridge: Cambridge University Press.
- Sullivan, A., Luo, J.-J., Hirst, A.C., Bi, D., Cai, W. and He, J. (2016) Robust contribution of decadal anomalies to the frequency of central-Pacific El Niño. *Scientific Reports*, 6, 38540. <https://doi.org/10.1038/srep38540>.
- Takahashi, K., Montecinos, A., Goubanova, K. and Dewitte, B. (2011) ENSO regimes: reinterpreting the Canonical and Modoki El Niño. *Geophysical Research Letters*, 38, L10707.
- Thom, H.C. (1966) *Some Methods of Climatological Analysis*. Geneva, Switzerland: World Meteorological Organization, Technical report 81.
- Torrence, C. and Compo, G.P. (1998) A practical guide to wavelet analysis. *Bulletin of the American Meteorological Society*, 79, 61–78. [https://doi.org/10.1175/1520-0477\(1998\)079<0061:APGTWA>2.0.CO;2](https://doi.org/10.1175/1520-0477(1998)079<0061:APGTWA>2.0.CO;2).
- Trenberth, K. and National Center for Atmospheric Research Staff. (2020) *The climate data guide: Niño SST indices (Niño 1+2, 3, 3.4, 4; ONI and TNI)*. Available at: <https://climatedataguide.ucar.edu/climate-data/nino-sst-indices-nino-12-3-34-4-oni-and-tni>
- Trenberth, K.E. (2006) The Impact of Climate Change and Variability on Heavy Precipitation, Floods, and Droughts. Anderson, M.G. & McDonnell, J.J., *Encyclopedia of Hydrological Sciences*. USA: John Wiley & Sons, Ltd.
- Urrea, V., Ochoa, A. and Mesa, O. (2019) Seasonality of rainfall in Colombia. *Water Resources Research*, 55, 4149–4162. <https://doi.org/10.1029/2018WR023316>.
- Valipour, M. (2015) Long-term runoff study using sarima and Arima models in the United States. *Meteorological Applications*, 22, 592–598. <https://doi.org/10.1002/met.1491>.
- Wang, C. (2007) Variability of the caribbean low-level jet and its relations to climate. *Climate Dynamics*, 29, 411–422. <https://doi.org/10.1007/s00382-007-0243-z>.
- Wang, C. and Fiedler, P.C. (2006) ENSO variability and the eastern tropical Pacific: a review. *Progress in Oceanography*, 69, 239–266.
- Wang, H.-J., Zhang, R.-H., Cole, J. and Chavez, F. (1999) El Niño and the related phenomenon southern oscillation (ENSO): the largest signal in interannual climate variation. *Proceedings of the National Academy of Sciences*, 96, 11071–11072. <https://doi.org/10.1073/pnas.96.20.11071>.
- Wei, W.W.S. (2006) *Time Series Analysis, Univariate and Multivariate Methods*, 2nd edition. Boston, MA: Pearson Addison Wesley.
- Xie, R., Mu, M. and Fang, X. (2020) New indices for better understanding ENSO by incorporating convection sensitivity to sea surface temperature. *Journal of Climate*, 33, 7045–7061. <https://doi.org/10.1175/JCLI-D-19-0239.1>.
- Yepes, J., Poveda, G., Mejía, J.F., Moreno, L. and Rueda, C. (2019) CHOCO-JEX: a research experiment focused on the Chocó low-level jet over the far eastern Pacific and western Colombia. *Bulletin of the American Meteorological Society*, 100, 779–796.

SUPPORTING INFORMATION

Additional supporting information may be found in the online version of the article at the publisher's website.

How to cite this article: Sayol, J.-M., Vásquez, L. M., Valencia, J. L., Linero-Cueto, J. R., García-García, D., Vigo, I., & Orfila, A. (2022). Extension and application of an observation-based local climate index aimed to anticipate the impact of El Niño–Southern Oscillation events on Colombia. *International Journal of Climatology*, 42(11), 5403–5429. <https://doi.org/10.1002/joc.7540>

APPENDIX A: OPERATIONAL IMPLEMENTATION OF TMI4

The promising results shown in this research have motivated the implementation of a semi-automatic procedure to compute and visualize the TMI4. It will allow to better test the applicability of TMI4 by the operational oceanography team of Centro de Investigaciones Oceanográficas e Hidrográficas del Pacífico, (Dimar-CCCP) under real time conditions.

First, input data (monthly time series of air temperature, SST, rain and sea level measured at Tumaco) are provided in columns within a single file with format .xlsx. Then the computation of TMI4 is launched by a script, in which the user is asked to give the path of the above .xlsx file. Once provided, the whole process is performed automatically in Python language (www.python.org, version 3.7.3): data standardization, PCA analysis and the computation of the 3-month moving average to obtain the TMI4. As discussed in section 4, the base period 1986–2015 has been selected. We note that this script only needs to be launched once per month, when new monthly data are available.

An accompanying visual interface also written in Python language over the graphic library wxpython (<https://wxpython.org>) is available (Figure A1). It is allocated in the server of the group of operational oceanography (AROPE), at Dimar-CCCP. This interface provides a plots selector that allows to choose which information is shown on the screen, such as the time series of standardized input data, time series of TMI4 (in which to make a zoom for desired periods is possible), and an operational table that contains the historical values of TMI4. Figures can be saved in .png format with a resolution of 350 dpi. As seen, values of TMI4 within the table are sometimes red or blue coloured. Colours are based on an operational protocol similar to the one used by NOAA (Kousky and Higgins, 2007). The intensity of the events is

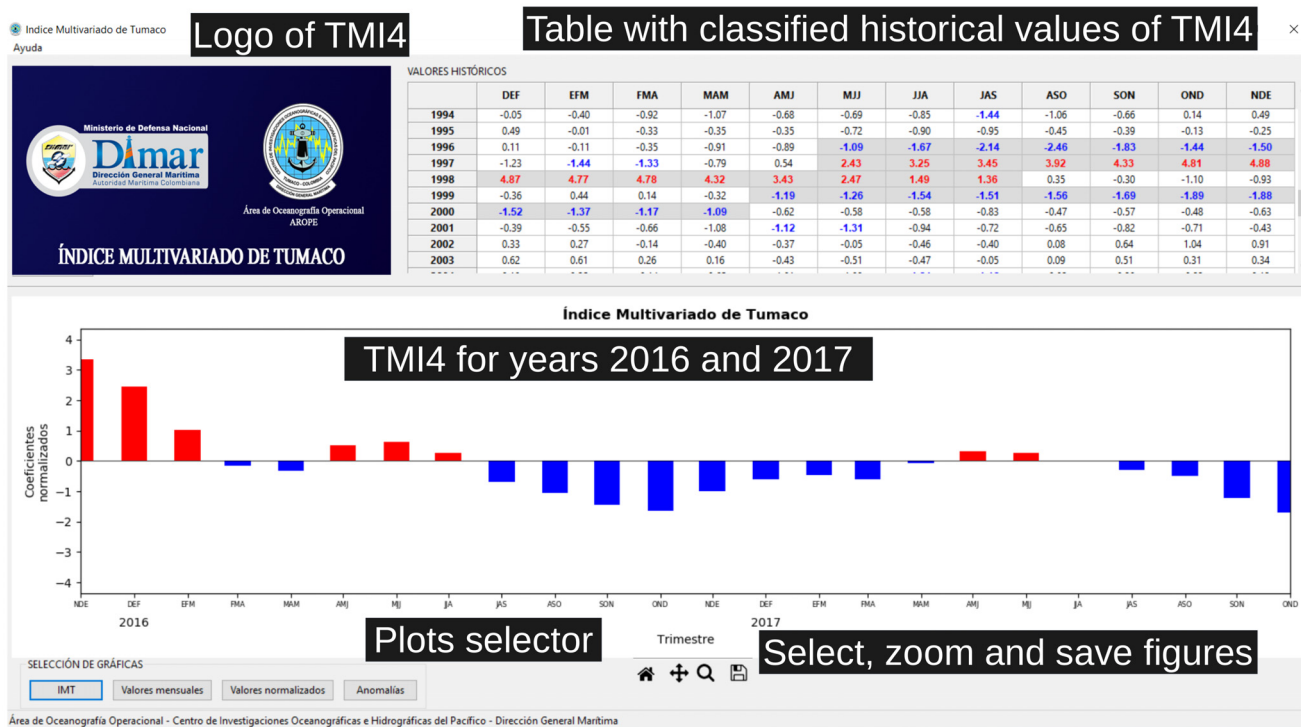


FIGURE A1 Snapshot of the visual interface of TMI4 developed at Dimar-CCCP. The interface includes a plot selector that can show time series of input variables and time series of TMI4. It is possible to zoom into time series for specific intervals of time (from a few months to several years). Also it is included a table with the historical values of TMI4. If values are above the thresholds defined in Table A1 they turn coloured (blue and red for La Niña and El Niño events, respectively). The interface is now being tested for operational purposes [Colour figure can be viewed at wileyonlinelibrary.com]

TABLE A1 The intensity of each value of TMI4 is operationally classified within range [Colour table can be viewed at wileyonlinelibrary.com]

Category	Range	Description
W5	$\geq 4\sigma_i$	Extremely warm
W4	$[3\sigma_i, 4\sigma_i)$	Very warm
W3	$[2\sigma_i, 3\sigma_i)$	Warm
W2	$[\sigma_i, 2\sigma_i)$	Moderately warm
W1	$(0, \sigma_i)$	Neutrally warm
C1	$(-\sigma_i, 0)$	Neutrally cold
C2	$(-2\sigma_i, -\sigma_i]$	Moderately cold
C3	$(-3\sigma_i, -2\sigma_i]$	Cold
C4	$(-4\sigma_i, -3\sigma_i]$	Very cold
C5	$\leq -4\sigma_i$	Extremely cold

Note: σ_i is defined in Table A2 and is different for each month i .

calculated according to the values of TMI4 in terms of the number of standard deviations (Table A1), for which the climatological monthly standard deviations of TMI4 are used (σ_i for the period 1961–2017, Table A2). Note that when the TMI4 is updated the values of σ_i are also

updated. However, as the time series of TMI4 is long (almost 60 years) changes in σ_i are expected to be fairly small at the scale of a few years. As an example of this classification, according to the scale in Table A1 the peak of El Niño 1998 reached category W5, while La Niña 2010

TABLE A2 Monthly standard deviations (σ_i , i refers to each month, $i = 1, \dots, 12$) used to classify TMI4 values in terms of ENSO events according to Table A1

i	DEF	EFM	FMA	MAM	AMJ	MJJ	JJA	JAS	ASO	SON	OND	NDJ
σ_i	1.24	1.12	1.09	1.08	1.09	1.04	1.05	1.06	1.08	1.18	1.33	1.36

had category C3. Regarding the persistence of the events, these are classified as conditions or episodes depending on their duration and their intensity. By conditions are referred those events that have three or less consecutive warm (values within W2–W5 category in

Table A1 and red colour in Figure A1) or cold (values within C2–C5 in Table A1 and blue colour in Figure A1) months. By episodes are referred those events that have at least four consecutive warm (El Niño) or cold (La Niña) months.